ARPA Order Number: 1408 Program Code Number: 9F10

Contract Number: DAHC19-69-C-0032

Contractor: The City College Research Foundation
The City College of the City University of New York
Convent Avenue at 138th Street
New York, New York 10031

Title: STRESS WAVE PROPAGATION THROUGH EARTH-WATER SYSTEMS
Second Project Report
Report No. 72-409-1
February, 1972

Principal Investigator: Professor Carl J. Costantino
212-621-2228

Contract Dates: 1 September 1969 to 31 August 1972

Amount of Contract: $76,123.

This Research was supported by the Advanced Research Projects Agency of the Department of Defense and was monitored by the U.S. Army Research Office under Contract No. DAHC19-69-C-0032.

64 R

Table of Contents

1.0 INTRODUCTION

This report is the first semi-annual report on Contract No. DAHC 19-69-C-0032 with the Advanced Research Projects Agency entitled "Stress-Wave Propagation Through Earth-Water Systems". The fundamental objective of this study is to develop numerical techniques to treat the general two-dimensional stress wave propagation problem through nonlinear earth materials including the effects of water flow through the earth materials.

Prior to the beginning of this study, a numerical technique was developed to treat the dynamic wave problem through arbitrary nonlinear media (Ref. 5, 6 and 7) without including the effects of water on the propagation process. This numerical approach is based upon the finite element method of analysis and led to the development of a large computer program (termed the SLAM Code for identification, the acronym standing for Stress Waves in Layered Arbitrary Media) to treat either the general axisymmetric or plane (stress or strain) geometric configuration. The finite element approach has been taken in this development to allow the user a general flexibility in treating two dimensional problems of rather complex geometry (inclusions, material layering, complex boundaries, etc.)

advantage can be considered a disadvantage for these cases.

After the development of SLAM Code, various problems of interest were investigated to determine the effects of material nonlinearities on the wave propagation process (Ref. 5). In general, two types of problems are of interest when studying dynamic processes through earth media. In the first type, the half space is subjected to high intensity pressure loadings caused by high energy explosions. The resulting ground shock effects are highly transient and are characterized by relatively short duration shock waves of high strength. Of particular interest for this problem is the rate of decay of the shock front as it moves through the ground. Clearly, nonlinear properties of the material significantly influence the decay of the shock strength since large nonrecoverable volume changes can decrease the peak pressures of the shock front. In the second problem type, the half-space is subjected to long duration low intensity vibratory type loadings associated with earthquake motions. Again nonlinear properties and volume changes of the earth material significantly alter the characteristics of the motion histories sustained at the surface of the ground.

In both of these problems, the stress and motion histories sustained at any point in the ground are significantly influenced by the nonlinear characteristics of the materials and the associated volume changes that occur. However, for real problems of interest, the soil/rock media often contains entrapped pore fluid which, due to its relatively high stiffness, will delay these

volume changes from occurring, the amount of the delay being controlled by the imperviousness of the earth material to water flow. Thus to seriously treat the time dependent response of earth media, the effects of pore water must be suitably taken into account.

In the following developments, the effects of pore water are included in the finite element analysis of SLAM Code with the eventual goal of treating the complete dynamic process. In the first effort presented herein, only the quasi-static problem is considered; that is, inertial effects are neglected. The problems of concern then are limited to (time-dependent) two dimensional consolidation situations including material nonlinearity effects. This course has been taken as a first step on the route to the complete development. The analyses and associated computer code developments can then be checked or compared with known solutions already available. At the end of this comparison phase, the inclusion of inertial effects can then be completed and solutions obtained for the various wave problems of interest.

2.0 GOVERNING SYSTEM EQUATIONS

In Ref. 1, the derivation of the system of equations governing both the equilibrium of the nodes as well as the pore pressure seepage condition (based on the two-dimensional Darcy's Law) were presented in detail. These relations can be written symbolically in matrix form as

(a) Equilibrium:

$$\{F_u\} = [k_{uu}]\{u\} + [k_{uw}]\{w\} - [\bar{k}_u]\{\pi\}$$

$$\{F_w\} = [k_{wu}]\{u\} + [k_{ww}]\{w\} - [\bar{k}_w]\{\pi\} \qquad (1)$$

(b) Seepage Flow:

$$\{P\} = [\bar{k}_u]^T\{\dot{u}\} + [\bar{k}_w]^T\{\dot{w}\} + [H]\{\pi\} \qquad (2)$$

In equations 1, the vectors $\{F_u\}$ and $\{F_w\}$ are the horizontal (u-direction) and vertical (w-direction) forces applied at the node points. The matrices k_{uu}, k_{uw}, k_{wu}, k_{ww} are the usual elastic stiffness matrices and are used to compute the elastic components of the forces developed at the node points due to relative displacements of the element nodes. The vectors $\{u\}$ and $\{w\}$ are the horizontal and vertical displacements of the nodes of the mesh, while the vector $\{\pi\}$ represents the excess pore pressures developed at the node points. The matrices $[\bar{k}_u]$ and $[\bar{k}_w]$ then convert the excess pore pressures developed at the nodes into equivalent node point forces.

The forces at the node points, $\{F_u\}$ and $\{F_w\}$, have two components, namely,

$$\{F_u\} = \{F_u^A\} + \{F_u^N\}$$

$$\{F_w\} = \{F_w^A\} + \{F_w^N\} \qquad (3)$$

where $\{F_u^A\}$, $\{F_w^A\}$ are the horizontal and vertical components of any forces applied to the nodes (from concentrated loads or pressures applied to specific surfaces in the problem). The forces $\{F_u^N\}$ and $\{F_w^N\}$ are the fictitious correction forces that are applied to the nodes to account for any nonlinearities in material stress-strain behavior (or deviations from the elastic case). For completeness of this report, the formulation of the matrices are presented in Appendix 1.

Equations 1 and 3 then represent the equilibrium of total stresses at a point in the half-space. Equation 2 represents the equation controlling the rate of seepage through the body and is obtained from Darcy's Law. The Matrix $[H]$ is dependent upon the coefficients of permeability of the earth material (as well as properties of the finite element configuration used) and the vectors $\{\dot{u}\}$ and $\{\dot{w}\}$ represent the horizontal and vertical node point velocities.

The vector $\{P\}$ represents the rate of volume change of the fluid associated with each node point. For incompressible fluid, these components are zero for interior node points (all fluid that flows into an element must flow out), while for some boundary node points (for which the excess pore pressure is zero), these components indicate the volume of water flowing out of the nodes. For compressible pore water (due to the fluid compressibility

itself or entrapped air), these components indicate the amount of volume change undergone by the fluid (see Ref. 1).

2.1 Solution Procedure

At each node point (except at boundary nodes where either displacements and/or excess pore pressures are specified), three unknowns must be determined at any instant of time, namely the two node displacements (u and w) and the excess pore pressure (π). The solution is then marched out in time in a step-by-step fashion. The integration procedure used to obtain the numerical results to be presented is based on a simple linear velocity approximation during a "small" time step or

$$\chi_i = \chi_{i-1} + \frac{\Delta t}{2}(\dot{\chi}_{i-1} + \dot{\chi}_i) \tag{4}$$

where χ_i represents a displacement at time i, χ_{i-1} the displacement at the previous time, $\dot{\chi}_i$ and $\dot{\chi}_{i-1}$ represent the corresponding velocities and Δt is the time increment between $i-1$ and i. Solving equation 4 for the current velocity

$$\dot{\chi}_i = -\dot{\chi}_{i-1} + \frac{2}{\Delta t}(\chi_i + \chi_{i-1}) \tag{5}$$

Substituting equation 5 into equation 2, the seepage equilibrium equation can be written as

$$\{G_i\} = -[\bar{k}_u]^T\{u_i\} - [\bar{k}_w]^T\{w_i\} - \frac{\Delta t}{2}[H]\{\pi_i\} \tag{6}$$

where the vector $\{G_i\}$ is defined as

$$\{G_i\} = -\frac{\Delta t}{2}\left(\{P_i\} + [\bar{k}_u]^T\left\{\dot{u}_{i-1} + \frac{2}{\Delta t}u_{i-1}\right\} + [\bar{k}_w]^T\left\{\dot{w}_{i-1} + \frac{2}{\Delta t}w_{i-1}\right\}\right) \tag{7}$$

The subscript i in equations 6 and 7 represents the current time and $i-1$ represents the previous time. At the current time, then, the system of equations to be solved can be written as

$$\begin{Bmatrix} F_u^A \\ F_w^A \\ G \end{Bmatrix}_i + \begin{Bmatrix} F_u^N \\ F_w^N \\ 0 \end{Bmatrix}_i = \begin{bmatrix} k_{uu} & k_{uw} & -\bar{k}_u \\ k_{wu} & k_{ww} & -\bar{k}_w \\ -\bar{k}_u^T & -\bar{k}_w^T & -\frac{\Delta t}{2}H \end{bmatrix} \begin{Bmatrix} u \\ w \\ \pi \end{Bmatrix}_i \tag{8}$$

or

$$\{F^A\}_i + \{F^N\}_i = [K]\{X\}_i \tag{9}$$

The matrix $[K]$ of equation 9 is symmetric, and the usual solution procedures can be used.

Considering an elastic porous material, at a particular time, the effective force vector of equation 9 is known. The applied loads are specified at the current time (F_u^A , F_w^A) and the force component G can be computed from equation 7 since the solution from the previous time step is known (obviously, the solution must start from a time when the initial conditions are specified). The unknowns (X_i of equation 9) can then be obtained by, say, a simple elimination technique. The solution at the following time

step can then be obtained using the current solution as input, etc. In this fashion, the solution is marched out in time.

For nonlinear material behavior, this process has to be modified since the nonlinear correction forces (F^N_u , F^N_w) of equation 8 are also functions of the current displacements. To overcome this situation, a modification of the above procedure is necessary. An initial trial solution is first obtained by using approximate values for these correction forces (usually the forces from the previous time step). An iteration procedure is then superimposed at each time step to check the adequacy of the trial nonlinear force correction terms.

3.0 NUMERICAL RESULTS

With the developed computer program, numerical results were generated for several soil configurations similar to the usual soil tests, consolidation and triaxial compression. The first set of data assumed elastic soil behavior, since for these problems analytic solutions are available or can be easily developed for comparison purposes. The first nonlinear soil model investigated made use of a Coulomb-Mohr elastic plastic model based on the concepts of the theory of plasticity.

Although this model is often used, it is not adequate for modeling stress-strain behavior (except in a crude sense) and would be of questionable value when studying pore pressure dependent problems. A more detailed soil model was then investigated which adequately predicts stress strain behavior of a particular sand sample and was developed by fitting the parameters of this model to available experimental data.

3.1 One-Dimensional Elastic Consolidation

The first problem investigated was, naturally, that of the classical one-dimensional consolidation of elastic material. The analytic solution available for comparison is the standard Terzaghi solution (Ref. 2). The problem parameters chosen for the investigation are shown in Figure 1. The computed settlement-time history at the top of the soil surface is shown in Fig. 2 and comparisons made with the exact analytic solution. The excess pore pressures developed at the bottom of the layer are shown in Figure 3

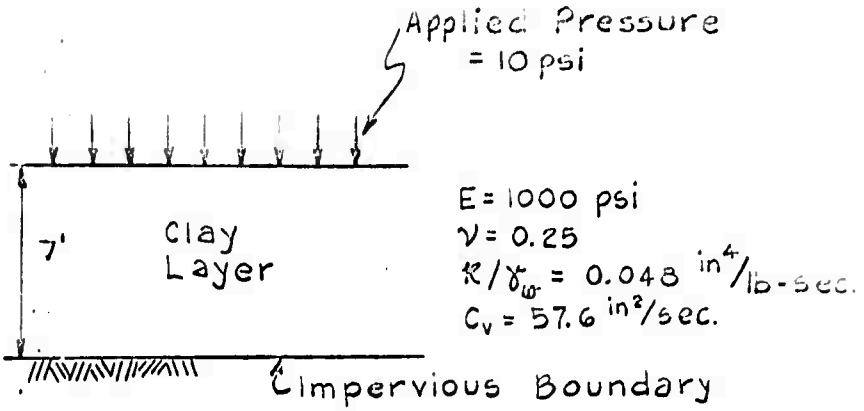

(a) Configuration Analyzed

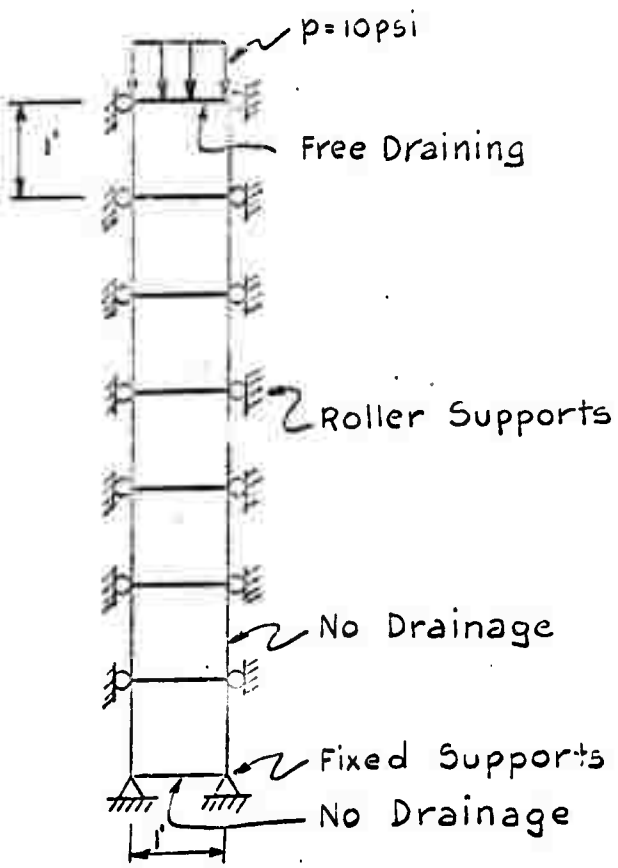

(b) Finite Element Configuration

Fig. 1 One-Dimensional Elastic Consolidation Problem

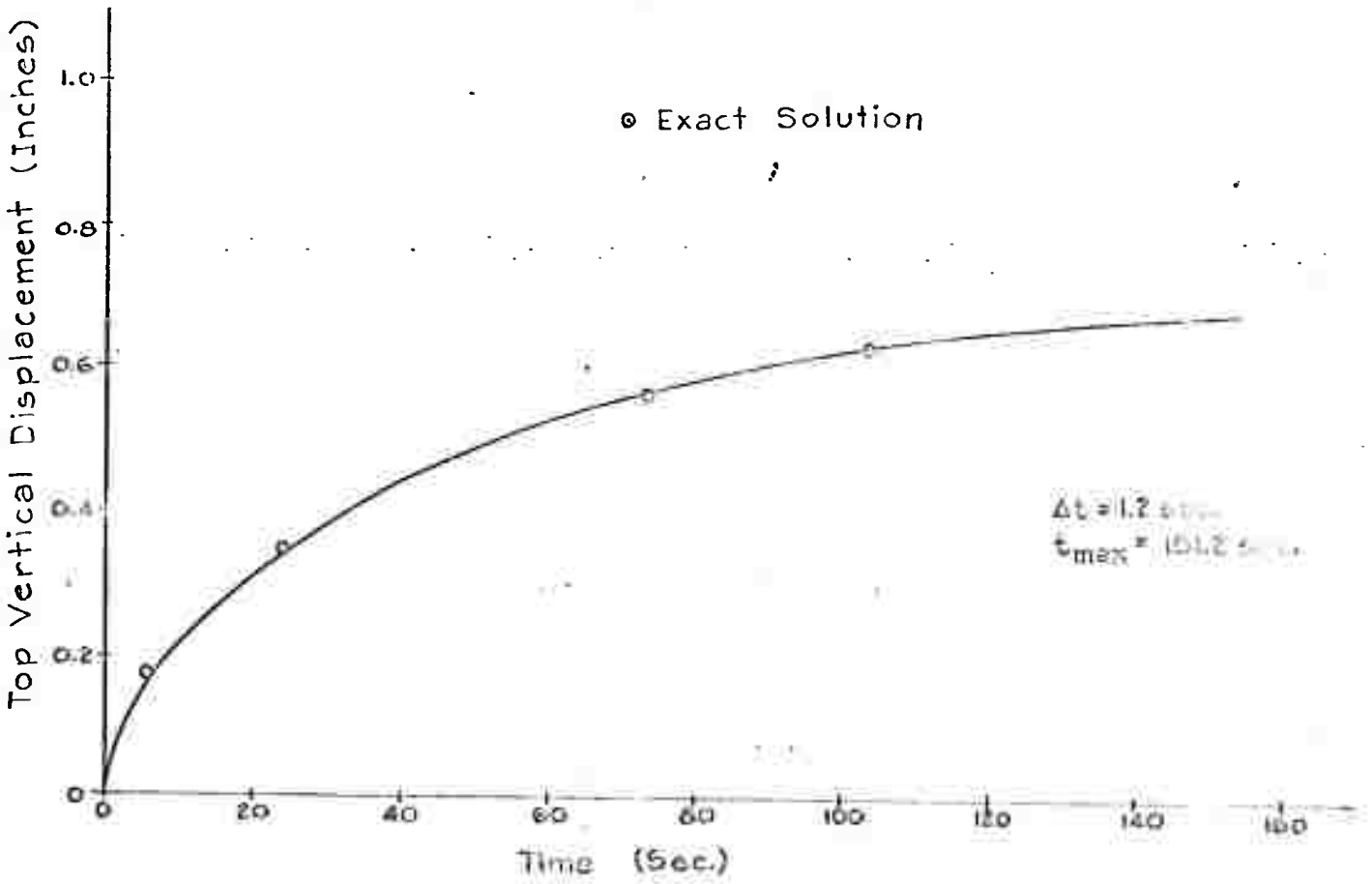

Fig. 2 One Dimensional Elastic Consolidation, Settlement of Top of Layer

while those at a point nearer the surface are shown in Figure 4. Again comparisons are made with the exact solution and in all cases they show excellent agreement. The pore pressure distribution at various times through the layer is shown in Figure 5. Since the pore pressure is assumed to vary linearly within a given element the distribution curves are piecewise linear. If in the actual problem the pore pressure variation is sharp, smaller element sizes must be used to suitably approximate the solution.

3.2 Triaxial Elastic Soil Configuration

The second model considered was the triaxial soil configuration shown in Fig. 6a. The soil model was considered to be elastic and a 50 psi vertical pressure applied at the initial or zero time. The finite element model used is shown in Fig. 6b and consists of 28 rectangular elements to represent the upper quarter of the triaxial sample. The elements are thus axisymmetric or ring elements.

To obtain the analytic solution, it was assumed that strain conditions in the sample are uniform. The initial pore pressure developed in the sample (prior to drainage occurring) is found from the following analysis. The volume change per unit soil volume for the elastic soil is

$$\Delta V = \frac{1-2\nu}{E}\left[\bar{\sigma}_r + \bar{\sigma}_\theta + \bar{\sigma}_z\right] \qquad (10)$$

where the barred stresses represent the intergranular stresses, and

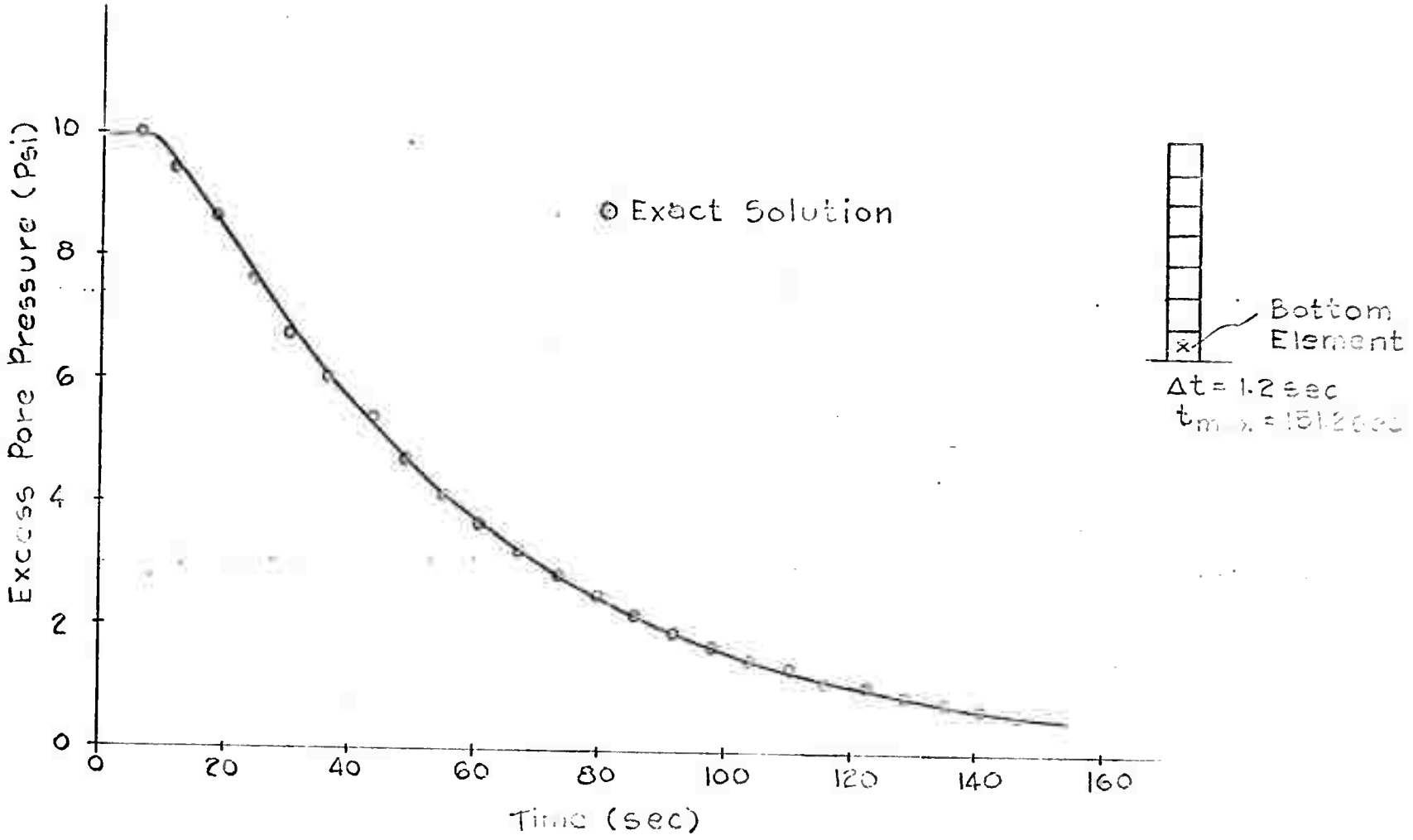

Fig. 3 One Dimensional Elastic Consolidation,

Excess Pore Pressure at Bottom Element

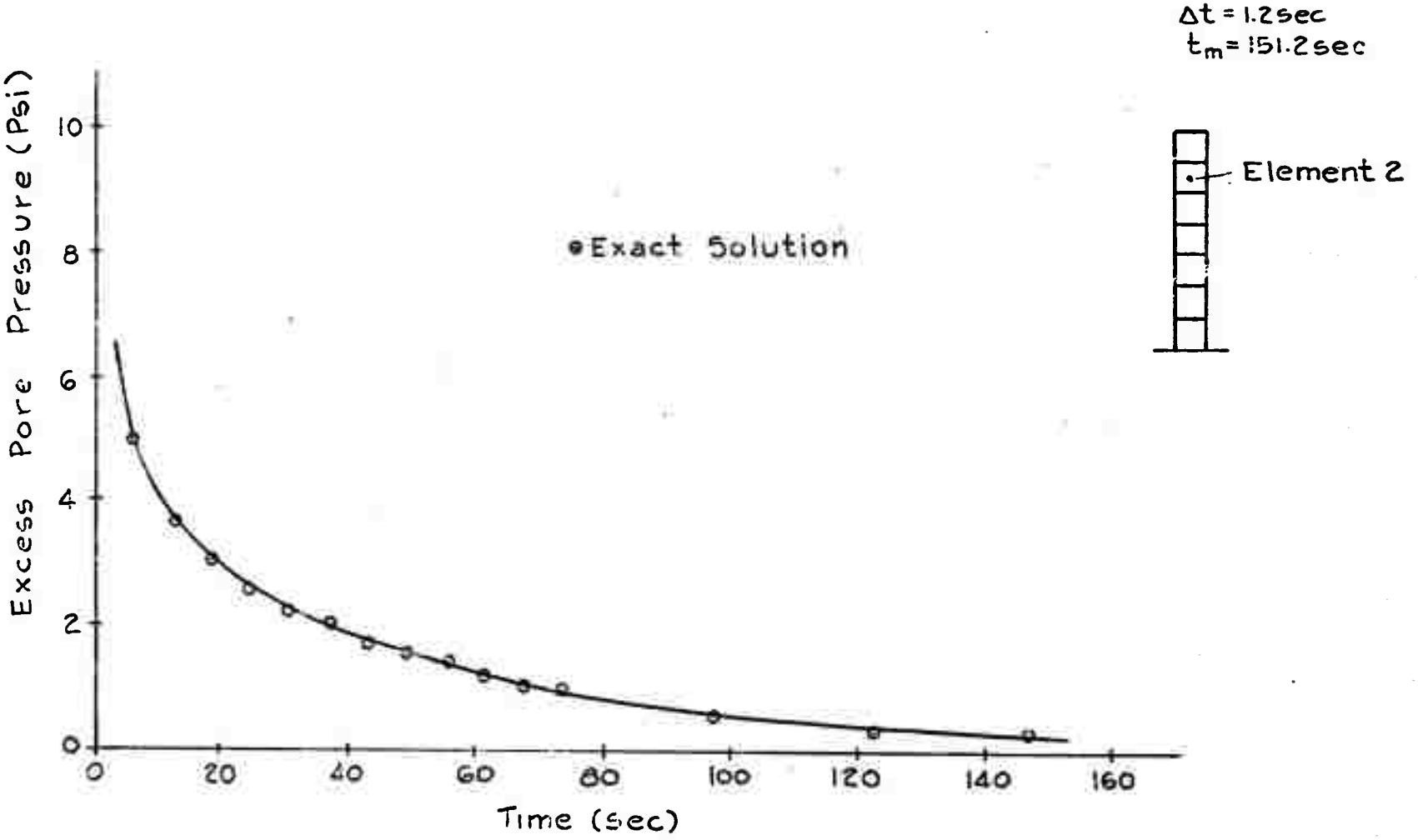

Fig. 4 One Dimensional Elastic Consolidation,
Excess Pore Pressure at 2nd Element

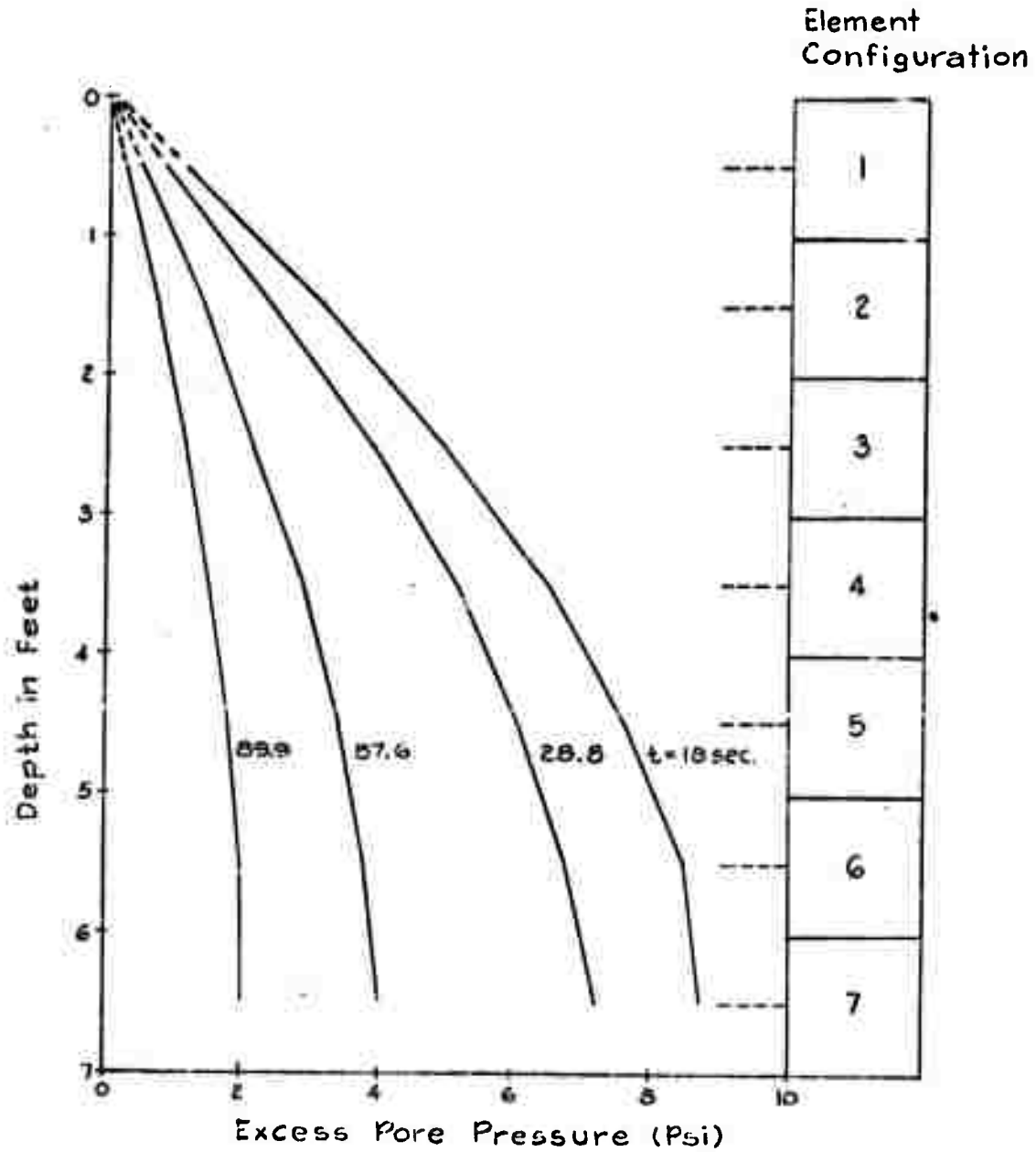

Fig. 5 One-Dimensional Elastic Consolidation, Excess Pore Pressure Distribution

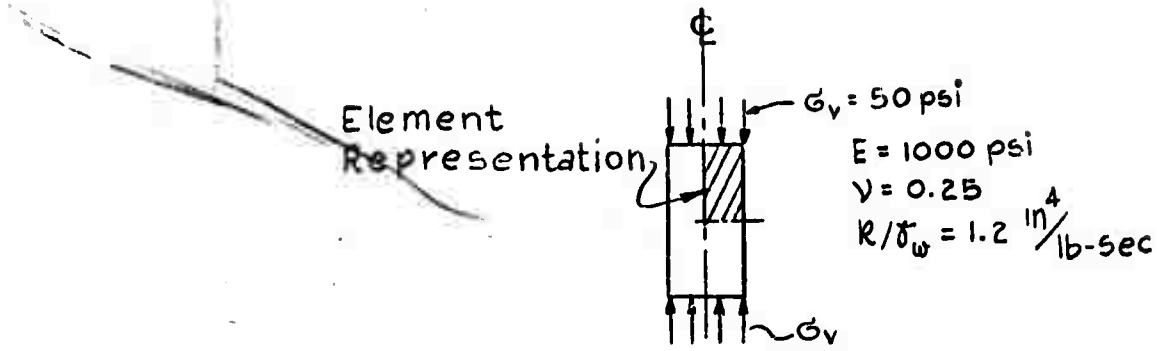

(a) Configuration of Triaxial Model

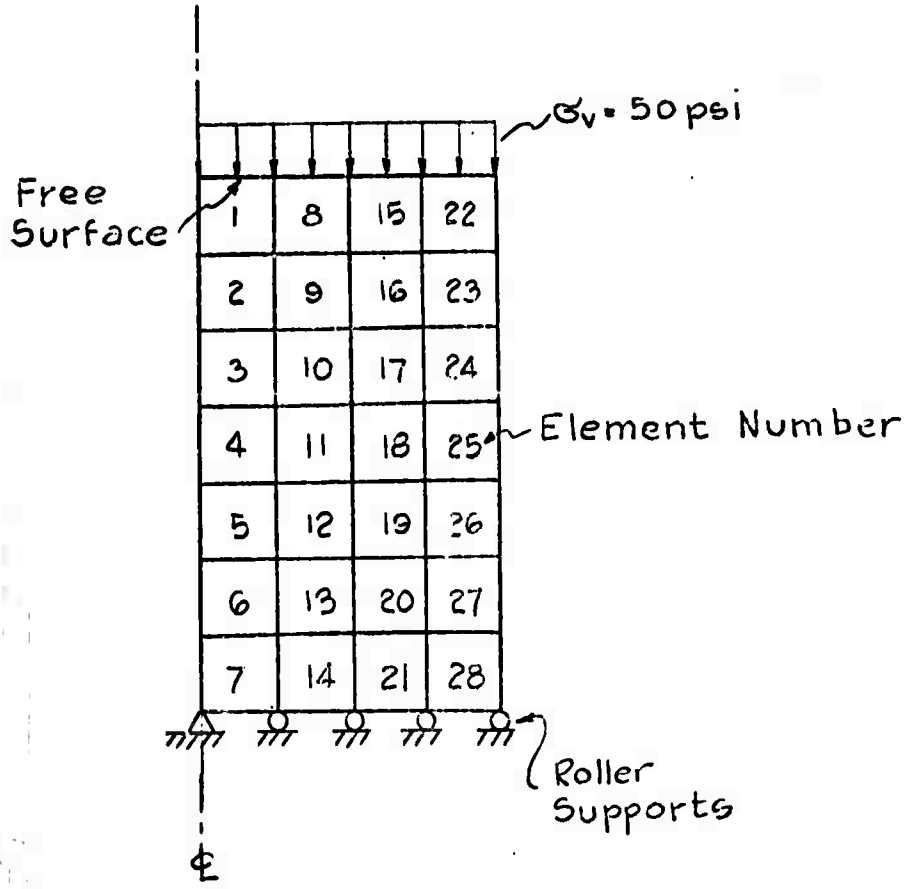

(b) Axisymetric Finite Element Model

Fig. 6 Elastic Triaxial Test Configuration

E and ν are the elastic modulus and Poisson's ratio, respectively. Since no seepage occurs during the initial conditions, the volume change is zero or

$$\bar{\sigma}_3 = -(\bar{\sigma}_r + \bar{\sigma}_\theta) \tag{11}$$

In addition,

$$\bar{\sigma}_r = \bar{\sigma}_\theta = -p$$

$$\bar{\sigma}_3 + p = \sigma_v \tag{12}$$

where p is the excess pore pressure and σ_v is the vertical applied stress. Combining equations 11 and 12 leads to the solution

$$\bar{\sigma}_3 = 2\sigma_v/3 \tag{13}$$

$$p = \sigma_v/3$$

The initial compression of the soil sample is simply

$$\Delta_i = \frac{2}{3}\,\frac{\sigma_v L}{E}\,(1+\nu) \tag{14}$$

The final stresses in the soil system are obtained when p is zero (no pore pressure) and

$$\bar{\sigma}_r = \bar{\sigma}_\theta = 0$$

$$\bar{\sigma}_3 = \sigma_v \tag{15}$$

while the final compression of the soil sample is

$$\Delta_f = \frac{\sigma_{vf} L}{E} \tag{16}$$

where L is half the original sample height (height of the finite element model). The settlement from the initial condition to the final condition is governed by the one-dimensional consolidation model (since one-dimensional seepage occurs through the top surface only) with the modification that the definition of the coefficient of consolidation is

$$C_v = \frac{k}{\gamma_w} \frac{E}{3(1-2\nu)} \tag{17}$$

The solution to the particular problem of Fig. 6 was obtained numerically using a time increment of 0.1 seconds. The pore pressure distribution along the centerline elements is shown in Fig. 7 together with comparisons with the analytic solution. As can be seen, the comparisons are excellent, except during the early part of the solution. In an attempt to uncover the cause of the discrepancies, the same problem was investigated with differing time increments, and the results are shown in Fig. 8. As may be noted by comparing Figs. 7 and 8, the early time oscillations found for the top element (Element 1) are related to the time step. As the time step is decreased, the oscillations disappear. A comparison with the exact solution shows that the computed solution is slightly lower and this can be attributed to the fact that the pore

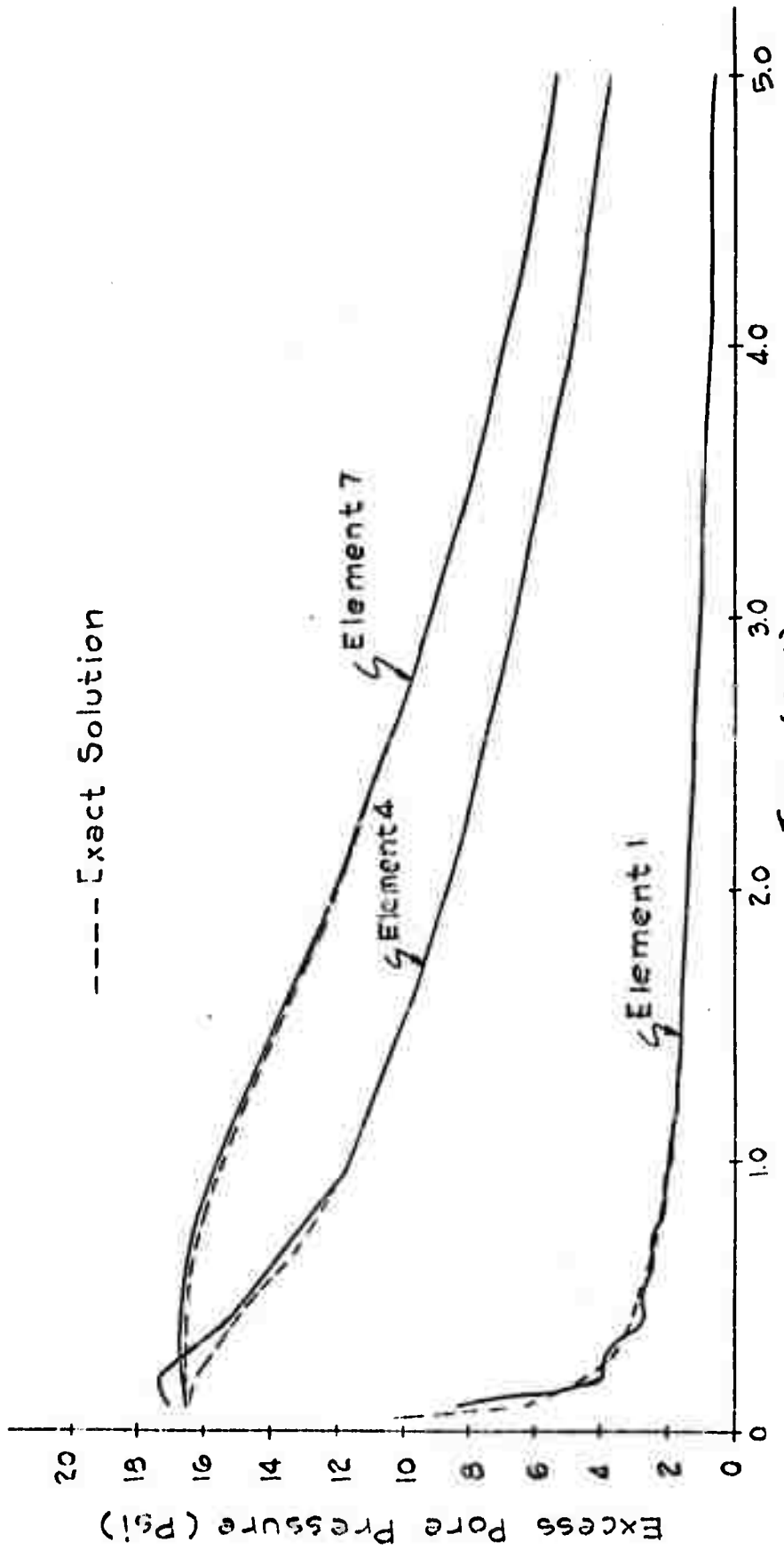

Fig. 7 Elastic Triaxial Test, Excess Pore Pressure Near Centerline

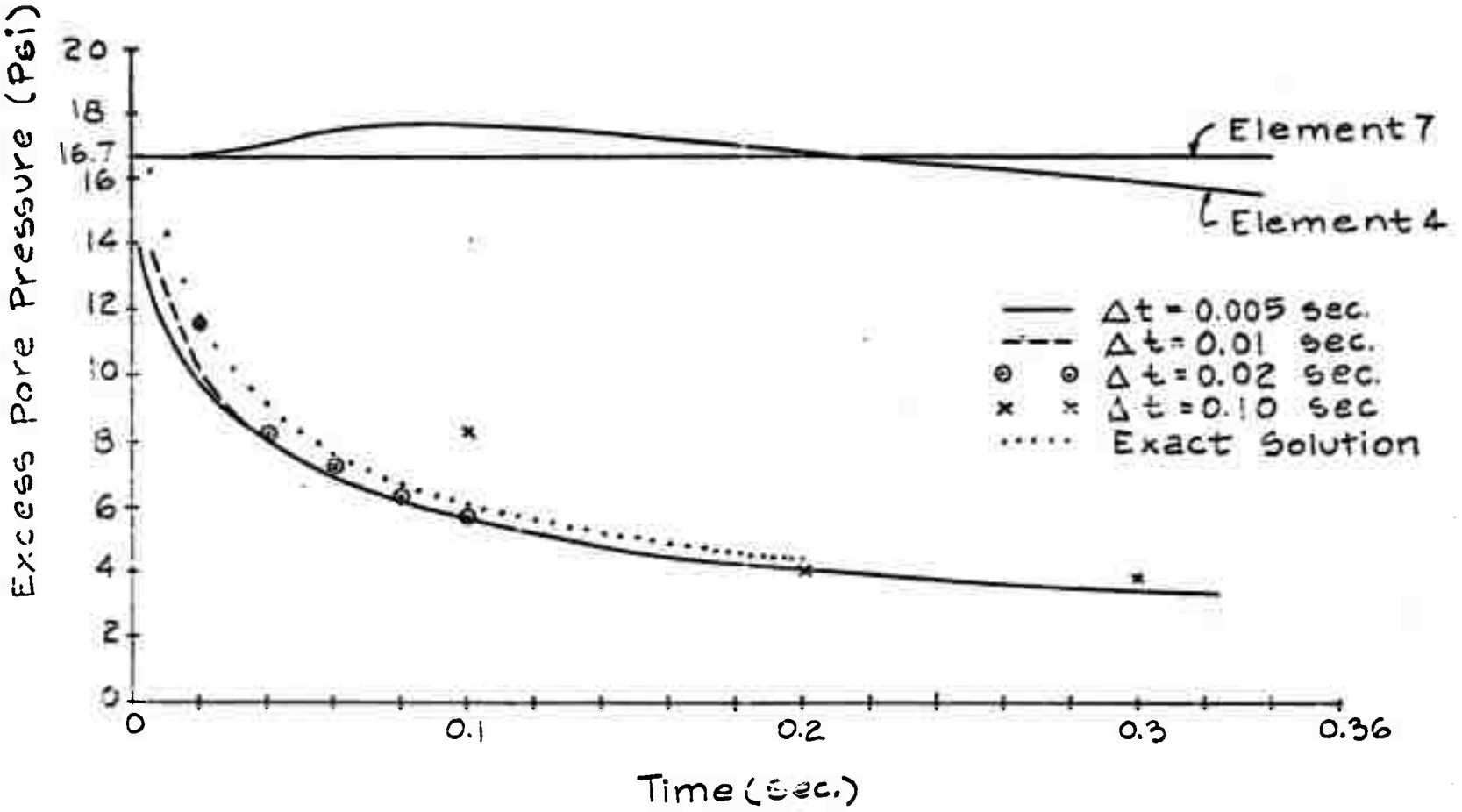

Fig. 8 Elastic Triaxial Solution, Excess Pore Pressure Near Centerline, Influence of Time Increment on Solution

pressure profile is assumed to be linear across the element while the actual pressure profile is curved, particularly at the early times.

The comparison with the middle element (Element 4) is not as clear cut, however. As may be noted from Fig. 8, this pore pressure shows an initial increase in pore pressure before the anticipated decay occurs, and this increase is independent of time increment of the integration. Since this phenomenon did not occur in the elastic plane problem discussed previously, it must be concluded that this variation is concerned with the coarseness of the finite element mesh in the radial direction for this axisymmetric problem. No further numerical studies have been conducted on this problem as yet, however.

3.3 Triaxial Coulomb-Mohr Model

The first triaxial problem including nonlinear material properties that was investigated was the same model shown in Fig. 6 but with nonlinear properties described by the Coulomb-Mohr yield condition (Ref. 3). For stresses within the yield surface, the soil is assumed to behave elastically, where the yield surface is defined by

$$\alpha J_1 + \sqrt{J_2'} = k \tag{18}$$

For the axisymmetric stress condition of interest for this problem,

$$J_1 = \bar{\sigma}_r + \bar{\sigma}_\theta + \bar{\sigma}_z$$

$$J_2' = \frac{1}{6}\left\{(\bar{\sigma}_r - \bar{\sigma}_\theta)^2 + (\bar{\sigma}_\theta - \bar{\sigma}_z)^2 + (\bar{\sigma}_z - \bar{\sigma}_r)^2\right\} + \bar{\tau}_{rz}^2 \qquad (19)$$

where the bar again indicates intergranular stresses. The coefficients (α, k) are related to the usual strength parameters obtained from a triaxial test series, ϕ, the angle of internal friction, and c, the cohesion, by

$$\alpha = \frac{2}{\sqrt{3}} \frac{\sin\phi}{(3-\sin\phi)}$$

$$k = \frac{6c}{\sqrt{3}} \frac{\cos\phi}{(3-\sin\phi)} \qquad (20)$$

For stresses on the yield surface, plastic strain components are determined from the usual normality principal.

Prior to investigating this problem numerically, the analytic solution for the initial stress condition was obtained (no drainage allowed). As the vertical stress is slowly increased, the soil behaves elastically and the previous solution applies. Substituting equations 12 and 13 into equations 19 yields

$$J_1 = 0$$

$$J_2' = \frac{1}{\sqrt{3}} \sigma_N$$

For plastic yielding to begin, the critical vertical stress must reach the value

$$\sigma_N^y = \sqrt{3}\, k \tag{21}$$

For applied stresses larger than this critical value, plastic flow must be accounted for, making use of the normality relation (Ref. 3), which for this problem becomes

$$\begin{aligned} \dot{\epsilon}_r^p = \dot{\epsilon}_\theta^p &= -\alpha - \frac{1}{6\sqrt{J_2'}}\,(\bar{\sigma}_z - \bar{\sigma}_r) \\ \dot{\epsilon}_z^p &= -\alpha + \frac{1}{6\sqrt{J_2'}}\,(\bar{\sigma}_z - \bar{\sigma}_r) \end{aligned} \tag{22}$$

where $(\dot{\epsilon}_r^p, \dot{\epsilon}_z^p)$ are the radial and vertical components of the plastic strain rate vector. The plastic volume change is

$$\Delta V^p = -\frac{3\alpha}{\left(\frac{1}{\sqrt{3}} - \alpha\right)}\,\epsilon_z^p \tag{23}$$

where ϵ_z^p is the total plastic vertical strain, while the elastic volume change is

$$\Delta V^e = \left(\frac{1-2\nu}{E}\right)(\bar{\sigma}_z + 2\bar{\sigma}_r) \tag{24}$$

Knowing that the total volume change is zero (no drainage out of the sample is allowed), the solution can be readily obtained for any applied stresses greater than the critical, or

$$\bar{\sigma}_r = -p = \left(\frac{1-\sqrt{3}\alpha}{3\sqrt{3}\alpha}\right)\sigma_N - \frac{k}{3\alpha}$$

$$\bar{\sigma}_3 = \left(\frac{1+2\sqrt{3}\alpha}{3\sqrt{3}\alpha}\right)\sigma_N - \frac{k}{3\alpha}$$

$$\epsilon_3^P = \left(\frac{1-\sqrt{3}\alpha}{3\sqrt{3}\alpha}\right)\left(\frac{1-2\nu}{E}\right)(\bar{\sigma}_3 + 2\bar{\sigma}_r)$$

$$\epsilon_3^E = \frac{1}{E}(\bar{\sigma}_3 - 2\nu\bar{\sigma}_r) \qquad (25)$$

$$\epsilon_3^T = \epsilon_3^E + \epsilon_3^P$$

The results for a particular undrained case are shown in Fig. 9. The vertical pressure is applied "slowly" with a rise time of 50 seconds until it reaches a peak pressure of 50 psi. The particular properties of the soil chosen were

$$E = 1000 \text{ psi}$$
$$\nu = 0.25$$
$$c = 20.8 \text{ psi}$$
$$\phi = 30^\circ$$

For this condition the critical vertical stress is reached when σ_N is 43.4 psi and the corresponding pore pressure is 14.45 psi. As the vertical stress is increased to 50 psi, plastic flow takes place (along with plastic volume expansion) and the pore pressure reduces to 11.1 psi. Five computer runs were made for this problem using different time steps as seen in Fig. 9. In each case, the nonlinear

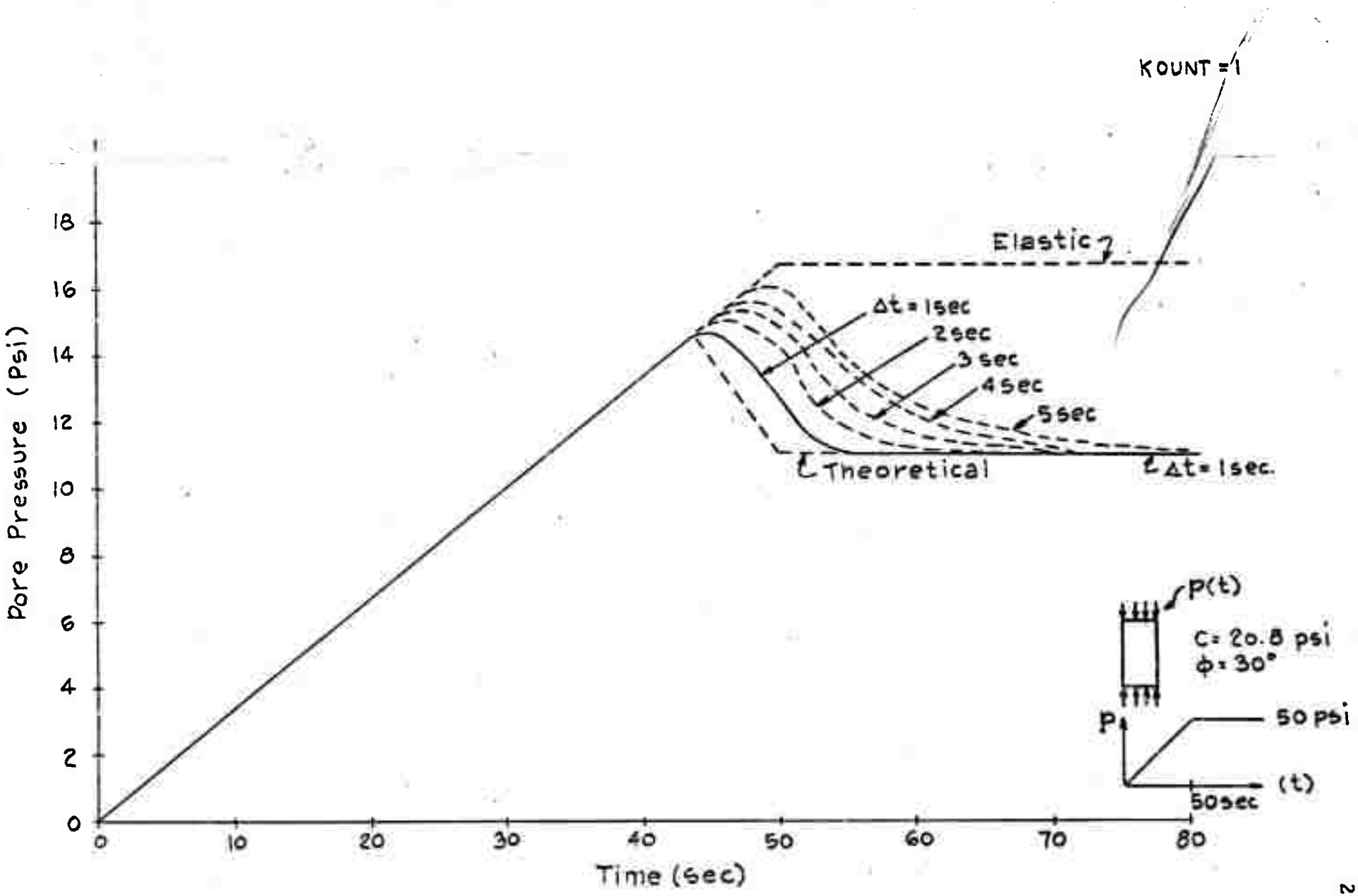

Fig. 9 Triaxial Compression, Coulomb-Mohr Material, Undrained Test

correction forces in the equilibrium equations were taken as the value computed during the previous time step. As can be noted, the smaller the time step, the better the approximation, as expected. As an alternate to this procedure, the nonlinear correction forces in a given time step can be recomputed by iteration (obtain a trial solution, computed correction force, obtain new solution, etc.). For this problem of proportional loading, this procedure is equivalent to using smaller time steps without iteration during each time step.

After the final equilibrium condition is reached under no drainage conditions, the drained situation can be achieved by letting the pore pressure decrease to zero by allowing drainage through the top and bottom surfaces of the soil sample. It can be shown that for this soil model, the decay of the pore pressure will occur elastically; that is, the intergranular stress state will move off the yield surface as the pore pressure decreases, so that the decay rate will be as described in the previous elastic triaxial solution.

The solutions for these cases are shown in Fig. 10 where the vertical intergranular stress is plotted as a function of the total vertical strain for various values of the cohesion and for a fixed value of the friction angle of 30°. If the cohesion is 24.0 psi or greater, the soil sample always remains elastic. The initial stress state when a vertical stress of 50 psi is applied and no drainage is allowed is $\bar{\sigma}_3$ = 33.3 psi and p = 16.7 psi. When drainage is then allowed, the pore pressure decreases to zero, and the vertical intergranular stress increases to the applied stress

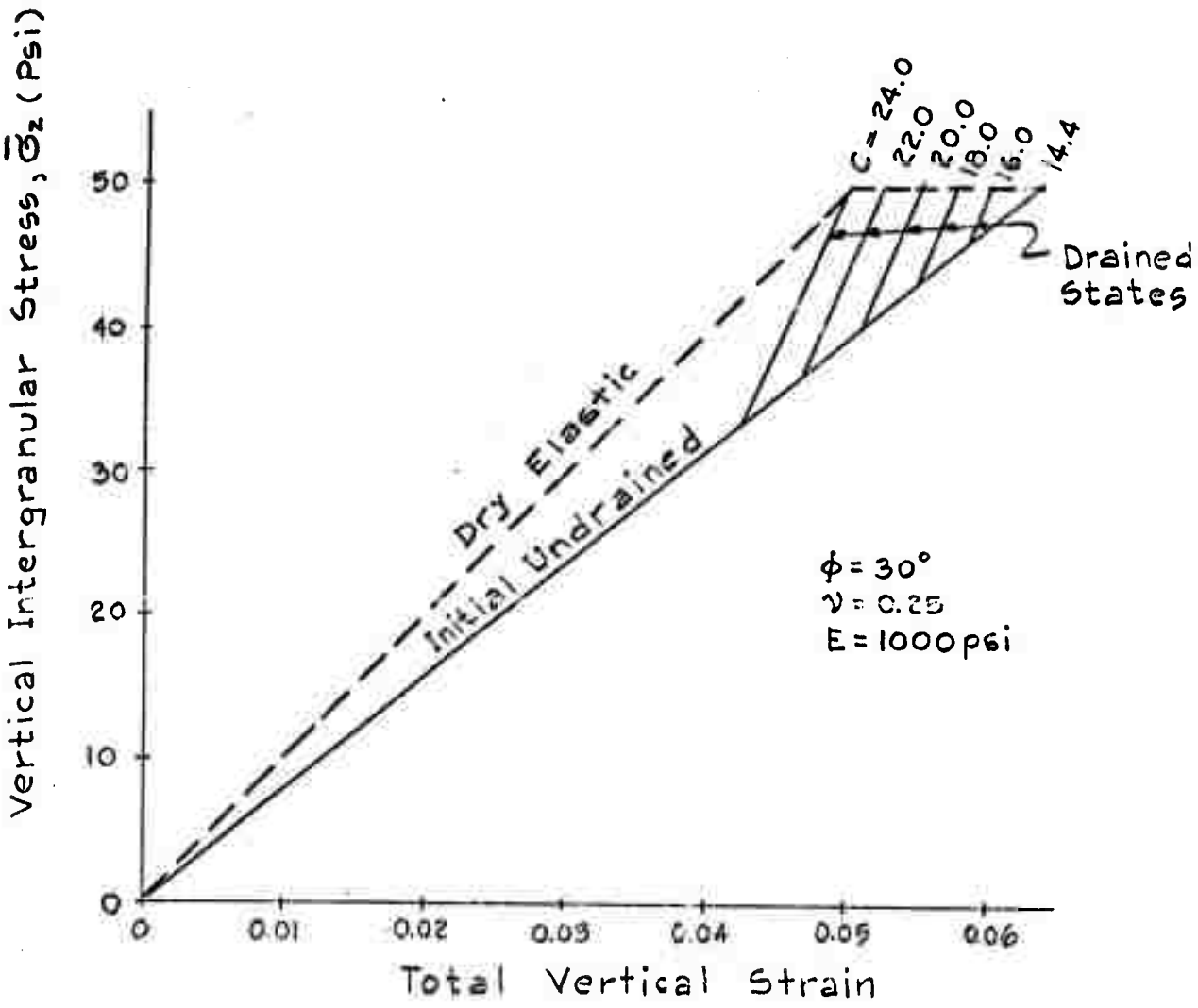

Fig. 10 Triaxial Compression Test, Coulomb-Mohr Material

of 50 psi. The final state is the same as would occur if the sample had been tested dry (no pore pressure). If, however, the cohesion is lower, the initial undrained state causes plastic flow to occur with the drained condition occurring elastically, as shown. For a value of cohesion equal to 14.4 psi, the initial undrained state occurs with no excess pore pressure, and the drained state is the same as the undrained state. For values of cohesion less than 14.4 psi, equilibrium under the applied loads cannot be maintained. It should be pointed out that for values of cohesion between 14.4 and 24.0 psi, the dry test will show no plastic flow, while the undrained-drained sequence will yield plastic strains.

It is clear then that even for this relatively simple soil model, the stress-strain behavior between saturated and unsaturated soil samples will be different and will be influenced by the rate of loading (as compared with the rate of pore pressure decay). To investigate this analytic solution further, the previous solution was nondimensionalized in the following fashion. Non dimensional parameters are defined as

$$\beta_1 = \frac{6}{\sqrt{3}} \frac{\cos\phi}{(3-\sin\phi)}$$

$$\beta_2 = \left(\frac{1+2\sqrt{3}\alpha}{3\sqrt{3}\alpha}\right) \qquad (26)$$

$$\beta_3 = \left(\frac{1-\sqrt{3}\alpha}{3\sqrt{3}\alpha}\right)$$

The upper and lower limits of cohesion for which a nonlinear solution (stable plastic strains will occur) can be obtained for the undrained case are

$$\left(\frac{c}{\sigma_{N_r}}\right)_u = \frac{1}{\sqrt{3}\,\beta_1}$$

$$\left(\frac{c}{\sigma_{N_r}}\right)_L = \frac{1}{\beta_1}\left(\frac{1}{\sqrt{3}} - \alpha\right) \qquad (27)$$

For any value of cohesion between these limits, the solution yields

$$\left(\frac{\bar{\sigma}_r}{\sigma_{N_r}}\right) = -\left(\frac{p}{\sigma_{N_r}}\right) = \beta_3 - \frac{\beta_1}{3\alpha}\left(\frac{c}{\sigma_{N_r}}\right)$$

$$\left(\frac{\bar{\sigma}_3}{\sigma_{N_r}}\right) = \beta_2 - \frac{\beta_1}{3\alpha}\left(\frac{c}{\sigma_{N_r}}\right)$$

$$\epsilon_3^E = \frac{\sigma_{N_r}}{E}\left\{\left(\frac{\bar{\sigma}_3}{\sigma_{N_r}}\right) - 2\nu\left(\frac{\bar{\sigma}_r}{\sigma_{N_r}}\right)\right\} \qquad (28)$$

$$\epsilon_3^P = \frac{\sigma_{N_r}}{E}\left\{\beta_3(1-2\nu)\left(\frac{\bar{\sigma}_3}{\sigma_{N_r}} + 2\,\frac{\bar{\sigma}_r}{\sigma_{N_r}}\right)\right\}$$

$$\epsilon_3^T = \epsilon_3^E + \epsilon_3^P$$

After this initial solution occurs, the addition vertical strain that will develop as the excess pore pressure is allowed to decay to zero is

$$\epsilon_z = \frac{\sigma_{N_r}}{E}\left\{(1-2\nu)\left(\frac{p}{\sigma_{N_r}}\right)\right\} \qquad (29)$$

so that the final strain is the sum of the strains from equations

28 and 29. The solutions for several parameter variations are shown in Figs. 11 through 14. In Fig. 11, the nondimensional vertical intergranular stress is plotted as a function of the ratio $\epsilon_3 / \epsilon_3^D$, where ϵ_3^D is the vertical strain that would occur in the dry state and is simply

$$\epsilon_3^D = \frac{\sigma_{N'}}{E} \tag{30}$$

As may be noted, the difference in limiting values of cohesion for this problem is relatively small, but the influence on the final strain is large (ratio of 6.25). Curves are shown for four equally spaced values of cohesion between the limiting values.

The same solution is shown in Fig. 12, except that the friction angle was increased from 5° to 30°. As may be noted, the final strains are much lower than those of Fig. 11, and the associated plastic strains occurring during the initial undrained state are much smaller. This is due to the fact that for the higher friction angle the plastic volume expansion is larger than for the smaller friction angle causing the excess pore pressure to decay more rapidly as plastic strains develop. Fig. 13 shows the same results for a still larger friction angle of 45°, again showing a smaller difference in final strains.

The results for a different value of Poisson's ratio ($\nu = 0.25$) are shown in Fig. 14 for a friction angle of 30°. As can be noted, the behavior is essentially different than that of Fig. 12. This is due to the fact that the elastic volume change

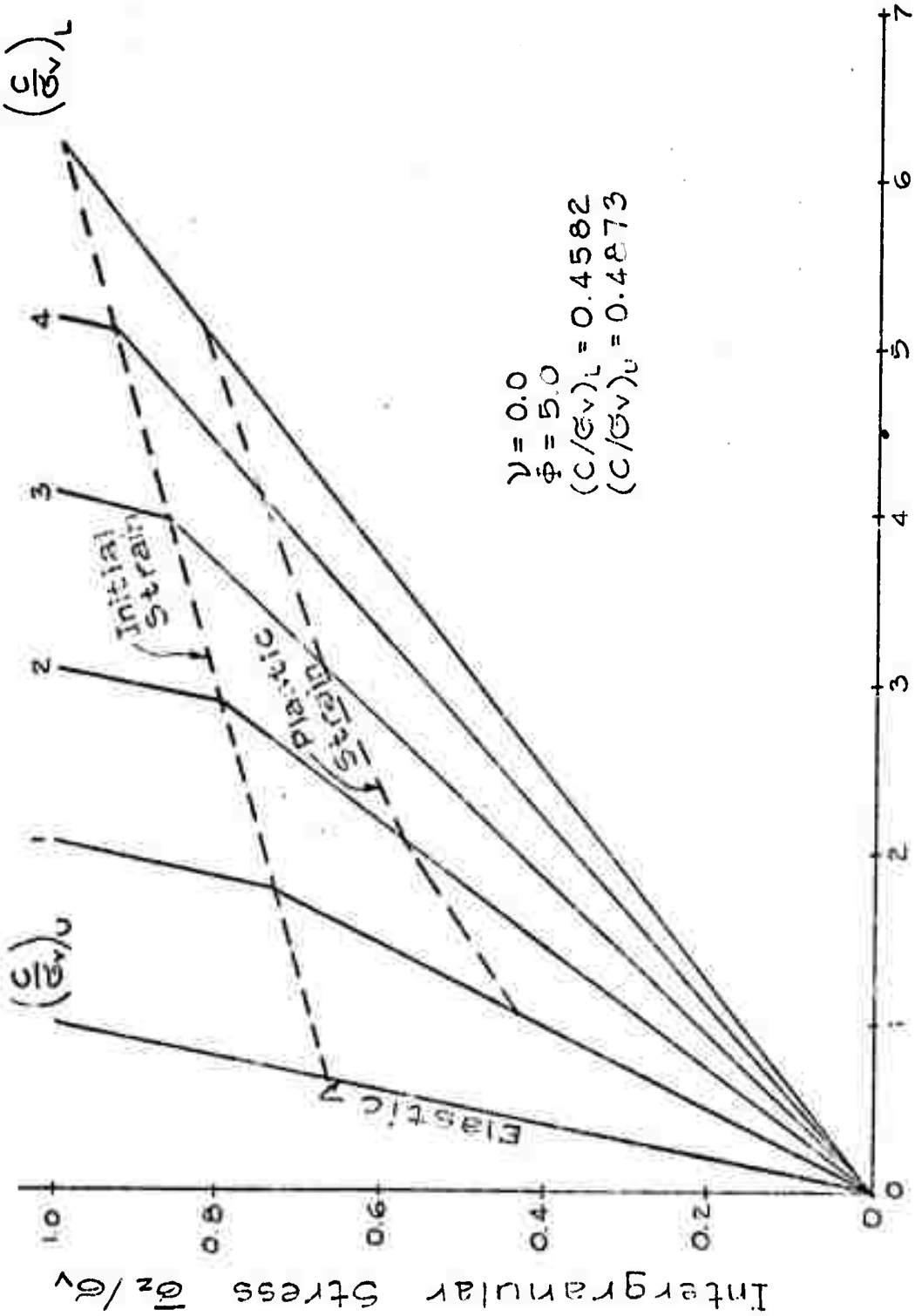

Fig. 11 Triaxial Compression Test, Coulomb-Mohr Material, Nondimensional Solution

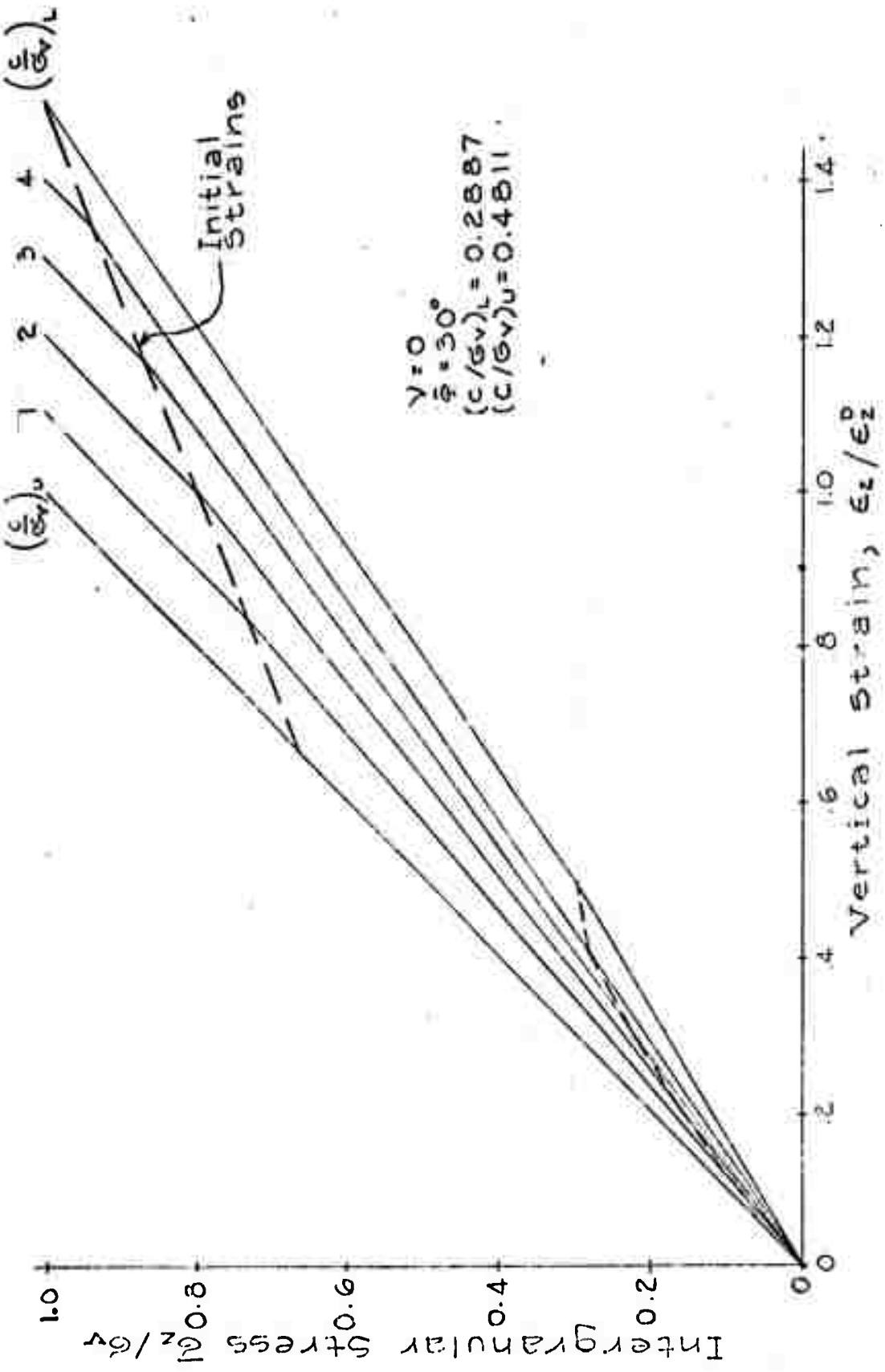

Fig. 12 Triaxial Compression Test, Coulomb-Mohr Material, Non-Dimensional Solution

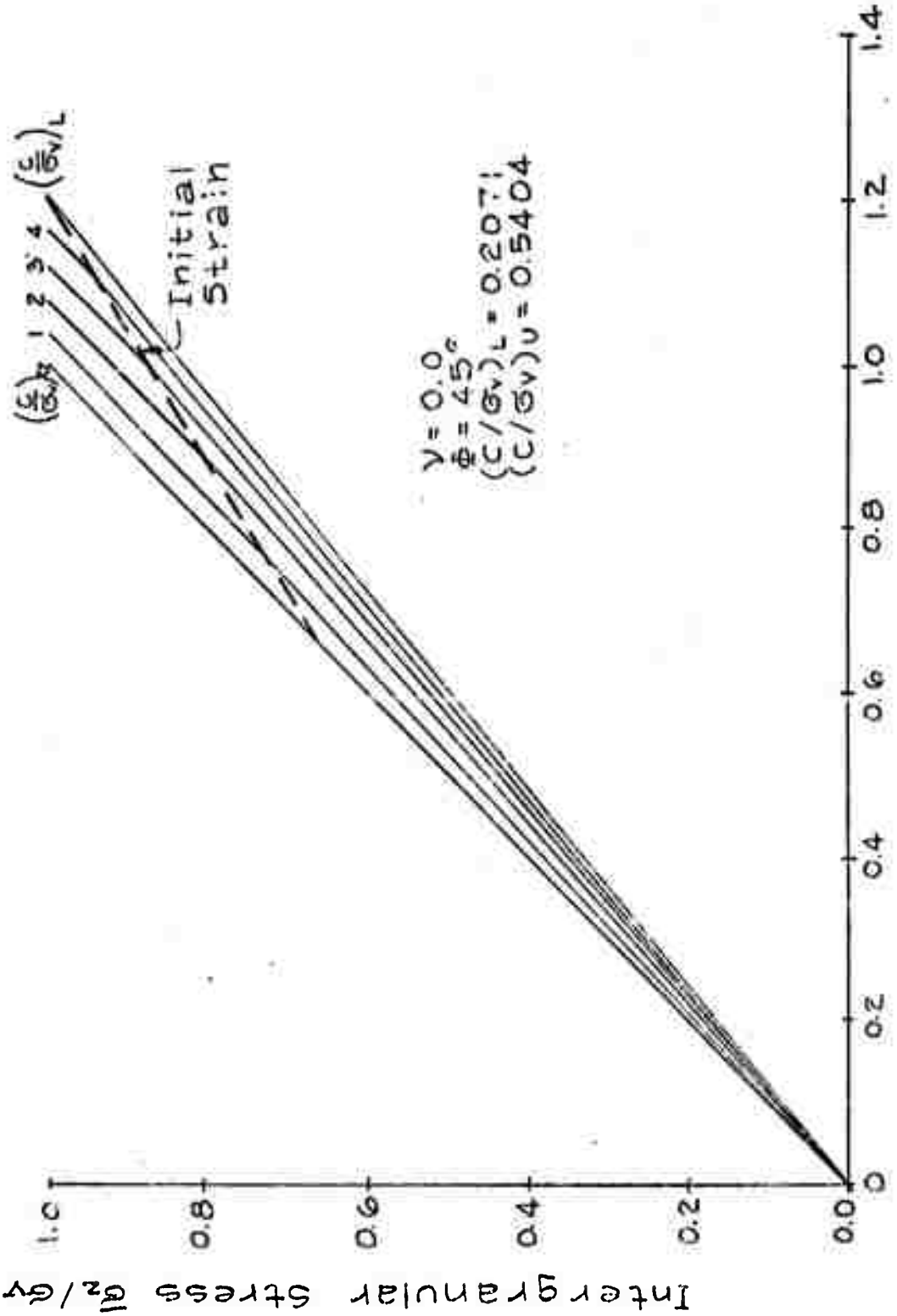

Fig. 13 Triaxial Compression Test, Coulomb-Mohr Material, Nondimensional Solution

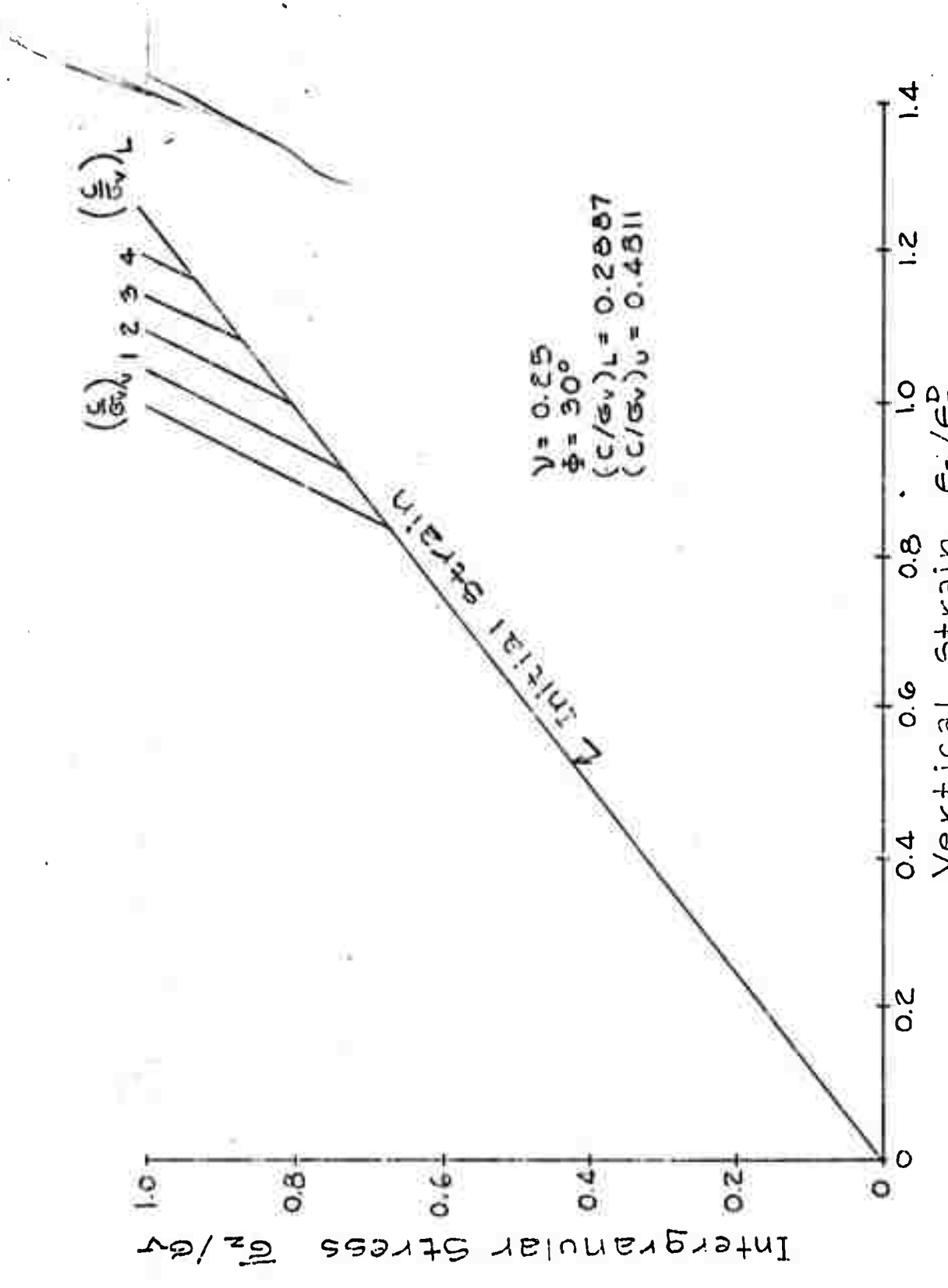

Fig. 14 Triaxial Compression Test, Coulomb-Mohr Material, Non-Dimensional Solution

during the initial loading decreases as Poisson's ratio increases.

3.4 McCormick Ranch Sand Model

It is, of course, well known that the relatively simplified constitutive models, such as the Coulomb-Mohr model, can only crudely approximate the stress-strain behavior of real soils. In order to properly take into account the influence of pore fluid on soil response, more realistic models must be developed. An example of such a model was presented in Ref. 4 wherein the parameters of the model were chosen to match (as closely as possible) available experimental data on a particular sand sample, known as McCormick Ranch Sand. A rather extensive series of triaxial, uniaxial, and hydrostatic compression tests were conducted and an attempt was made to fit the analytic model so as to reproduce the available data.

It was found that for the particular parameters chosen the stress-strain curve during the initial load-unload cycle could be adequately reproduced for the triaxial compression test (over a wide range of confining pressures) and for the uniaxial compression test. The soil model, however, was significantly stiffer under hydrostatic compression (although the shape of the load-unload curve was the same) than the experimental data.

The model is based on the following analysis. The hydrostatic and deviatoric stress-strain components are related by

$$\dot{s}_{ij} = 2G\,\dot{e}_{ij}$$

$$\dot{p} = 3K\,\dot{\varepsilon} \qquad (31)$$

where S_{ij} = deviatoric stress tensor

e_{ij} = deviatoric strain tensor

p = hydrostatic pressure

e = volumetric strain $= \frac{1}{3}(\dot{\epsilon}_1 + \dot{\epsilon}_2 + \dot{\epsilon}_3)$

and are related to the total stress-strain components by

$$\dot{e}_{ij} = \dot{\epsilon}_{ij} - \dot{e}\,\delta_{ij}$$

$$\dot{s}_{ij} = \dot{\sigma}_{ij} - \dot{p}\,\delta_{ij} \qquad (32)$$

where (σ_{ij}, ϵ_{ij}) are the total stress-strain tensors and δ_{ij} is the Kronecker delta. The dots in equations 31 and 32 indicate the corresponding rates. The parameters K and G represent the bulk and shear moduli, respectively, and are taken as functions of stress history.

The form used for the bulk modulus is:

loading: $K_L = K_0 + K_1 e + K_2 e^2$, for $\dot{e} > 0$ (33)

unloading: $K_u = K_{0u} + K_{1u} p$

where the parameters K_0, K_1, K_2, K_{0u}, K_{1u} are parameters found by fitting the experimental data. In equation 33, volume compression is assumed to be positive. The corresponding form used for the shear modulus is

loading:

$$G_L = G_0 + \bar{\gamma}_1\sqrt{J_2'} + \gamma_1 p + \gamma_2 p^2 \qquad \text{for } p \le p_c$$
$$= G_1 + \bar{\gamma}_1\sqrt{J_2'} \qquad \text{for } p > p_c \tag{34}$$

unloading:

$$G_u = G_{0u} + \bar{\gamma}_{1u}\sqrt{J_2'} + \gamma_{1u} p + \gamma_{2u} p^2 \qquad \text{for } p \le p_c$$
$$= G_{1u} + \bar{\gamma}_{1u}\sqrt{J_2'} \qquad \text{for } p > p_c$$

and

$$G_1 = G_0 - \frac{1}{4}\frac{\gamma_1^2}{\gamma_2}$$
$$G_{1u} = G_{0u} - \frac{1}{4}\frac{\gamma_1^2}{\gamma_2} \tag{35}$$

where p_c is a critical hydrostatic pressure (positive in compression and J_2' is the second invariant of the deviatoric stresses (equation 19).

To match the specific test results for the sand sample, the following parameters were found to best reproduce all the data:

$G_0 = 8.0$ ksi	$G_{0u} = 8.0$ ksi
$K_0 = 5.83$ ksi	$K_{0u} = 32.0$ ksi
$K_1 = 80$ ksi	$K_{1u} = 143$
$\gamma_1 = 32.4$	$\bar{\gamma}_1 = -110$
$\gamma_2 = -15.0$ 1/ksi	$K_2 = 30{,}000$ ksi
$\gamma_{1u} = 40.0$	$\gamma_{2u} = -18.5$ 1/ksi
$\bar{\gamma}_{1u} = 500.0$	

The stress-strain behavior under uniaxial compression is

shown in Fig. 15 under both initial loading conditions as well as strain load/unload cycling. As may be noted, the stress-strain response exhibits the characteristic stiffening effect as well as the nonrecoverable behavior under load cycling. The pressure ranges shown are higher than normally used but suitable modification of the data input would convert this typical response to lower stress ranges of interest.

The behavior under triaxial compression is presented in Figs. 16 to 19 and again exhibits much of the characteristics anticipated for a sand sample. During the load/unload cycling, the model can be further improved to reproduce test data by modifying the shear modulus formulation under reload conditions to better match strain behavior with constant load cycling.

The previous data were obtained for the Ranch Sand model in the dry condition. To determine the behavior with pore fluid, similar problems were investigated including load cycling effects. In Fig. 20, the triaxial response is presented for a consolidated/undrained experiment with load cycling in the vertical direction corresponding to the load cycles shown in Fig. 18 for the dry sample. In both cases, lateral or confining stresses were maintained constant. As can be seen in Fig. 20, the effect of pore pressure is to decrease the axial strain increment between load cycles. That is, in the undrained state, the soil model "shakes down" to effectively a linear model, although strong nonlinear behavior again takes effect as the applied load is finally increased beyond the load cycling regime.

Similar behavior is shown in Fig. 21 where the applied vertical load is cycled through the complete load range from 0 to 300 psi. This test corresponds to the dry triaxial test shown in Fig. 19. Again, it may be noted that within a load cycle, pore pressure effects cause the stress-strain behavior to "shake down" to an effective elastic state. Of course this type of response can be modified by changing the definition of the reload shear modulus as defined by equation 34. A plot of the invariants of effective stresses during the loading cycle for the triaxial tests is shown in Fig. 22, for both the consolidated undrained and drained tests. As may be noted, J_1 is constant during the undrained test indicating that the bulk modulus (equation 33) is constant with this model. Therefore the cycling response will be completely dependent upon the variation in the deviatoric response, or the shear modulus behavior. The cycling response will be essentially elastic as long as the shear modulus is maintained as the unloading modulus within the cycling load range.

Two other triaxial experiments were conducted where the samples were consolidated under a confining stress of 400 psi, loaded vertically in the drained state to 630 psi and then further loaded cycled between 575 psi and 690 psi in both the drained and undrained states. A comparison of the results is shown in Fig. 23, in which anticipated responses were determined.

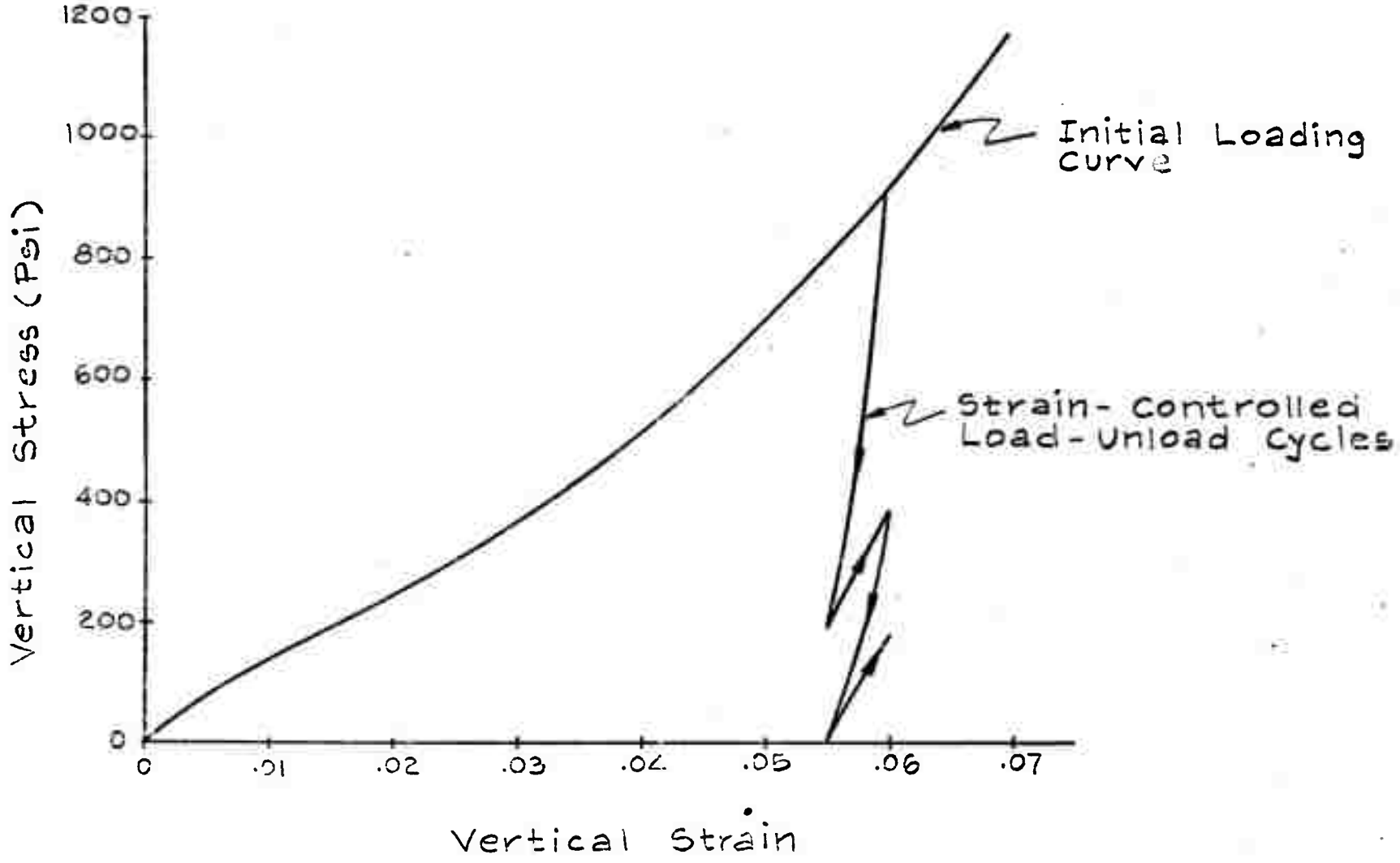

Fig. 15 Uniaxial Compression Test, Ranch Sand Model, No Pore Fluid

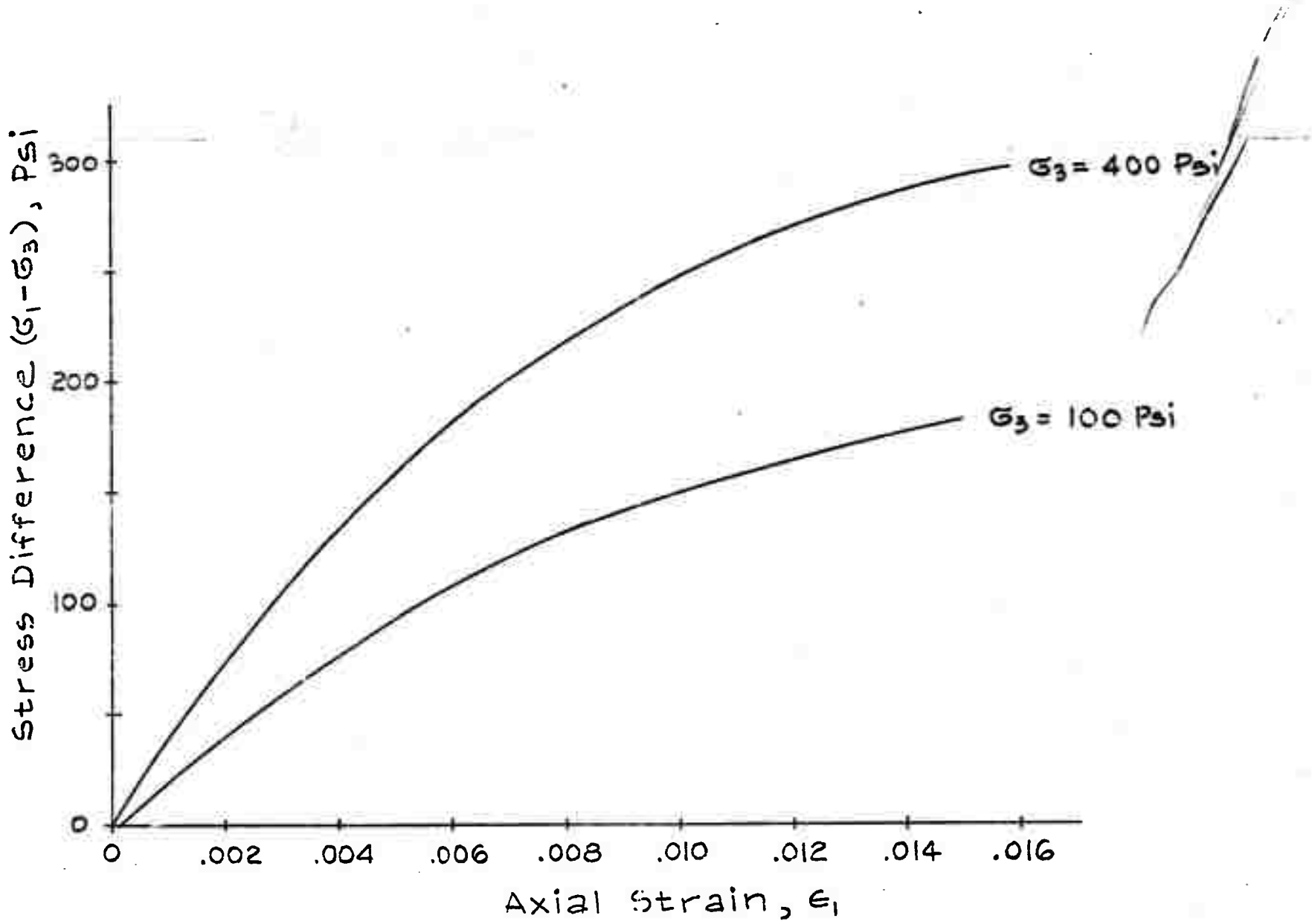

Fig. 16 Triaxial Response, Ranch Sand Model, No Pore Fluid

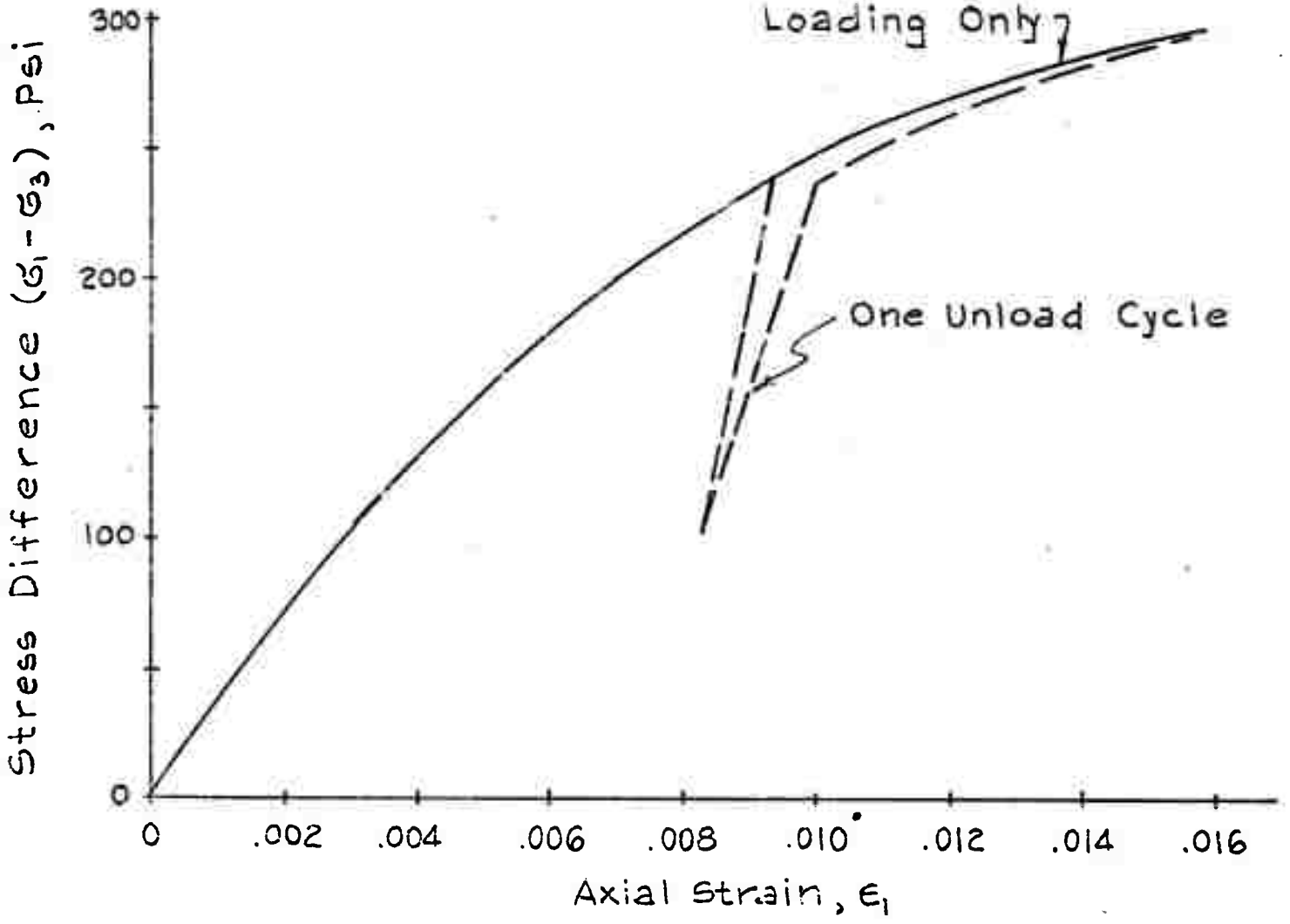

Fig. 17 Triaxial Response, Ranch Sand Model, No Pore Fluid

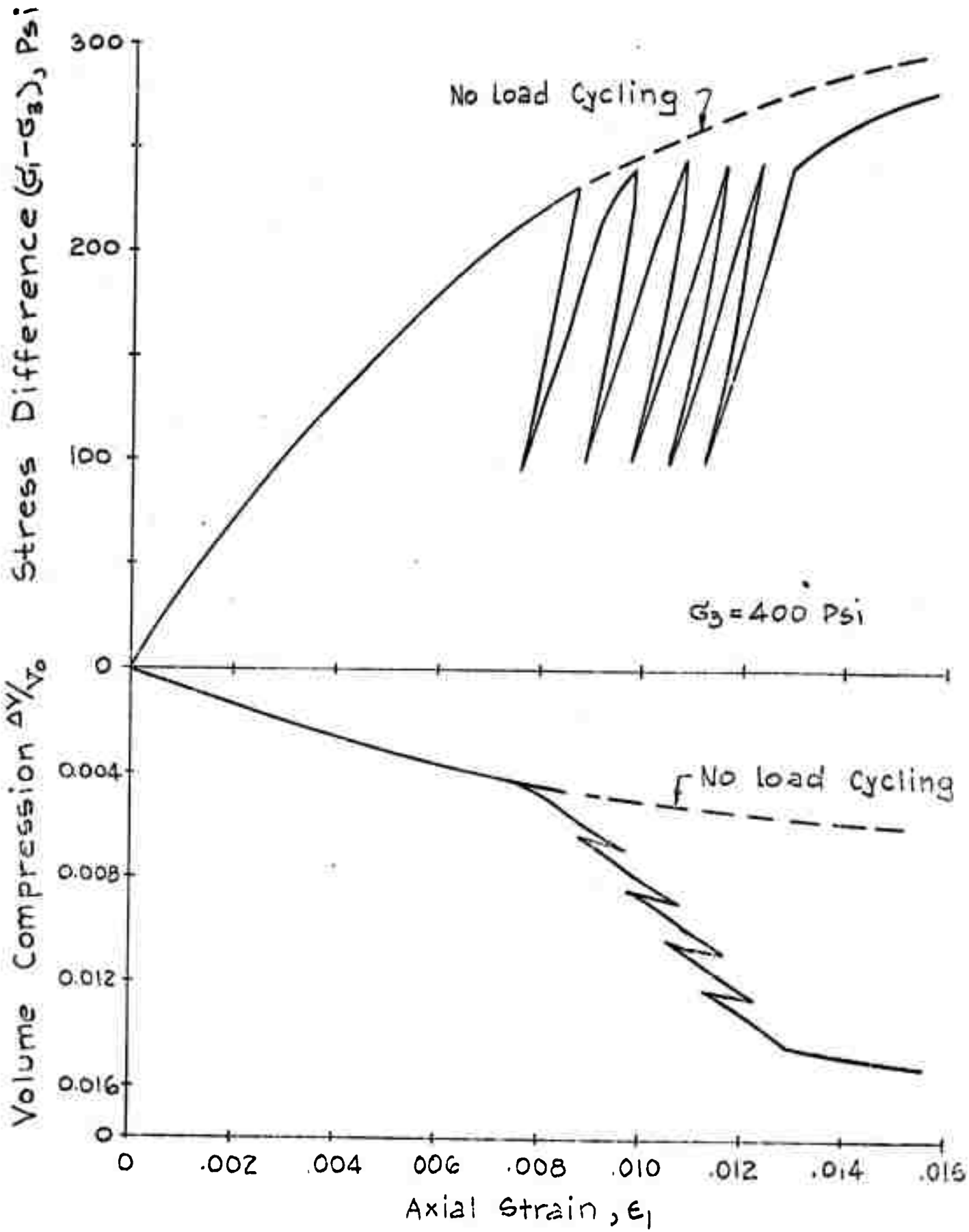

Fig. 18 Triaxial Response, Ranch Sand Model, No Pore Fluid

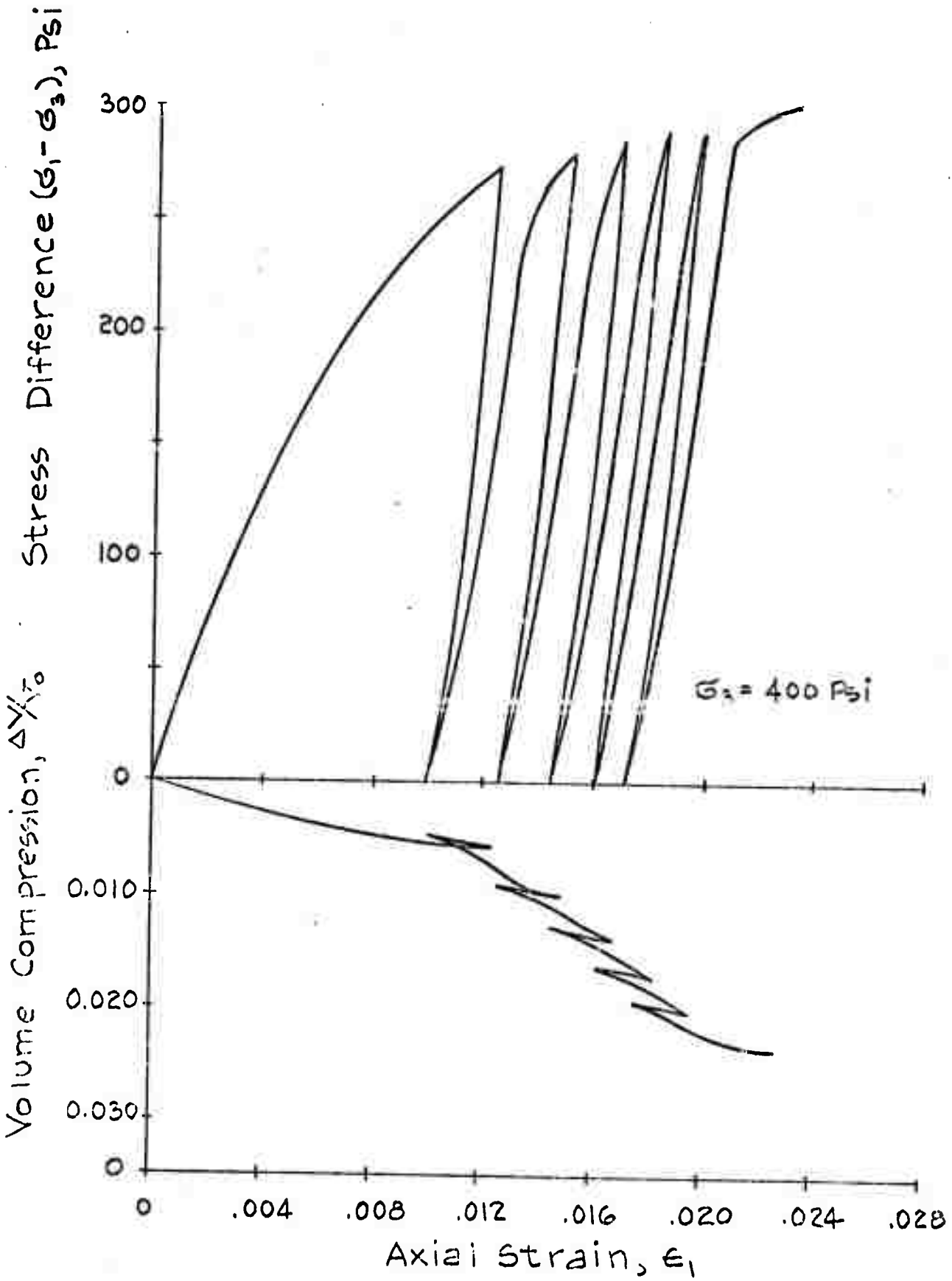

Fig. 19 Triaxial Response, Ranch Sand Model, No Pore Fluid

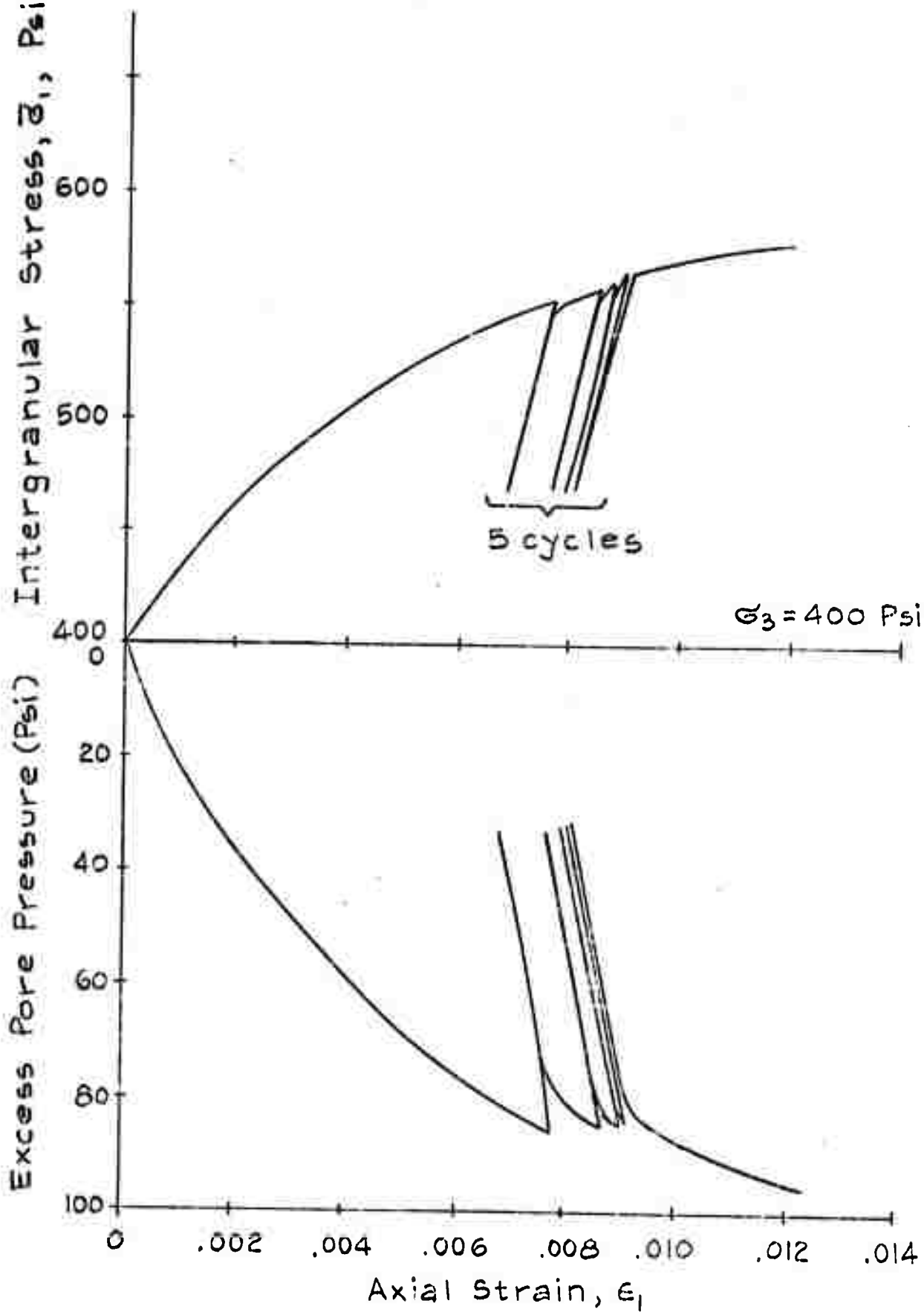

Fig. 20 Triaxial Response, Ranch Sand Model, Consolidated, Undrained Test

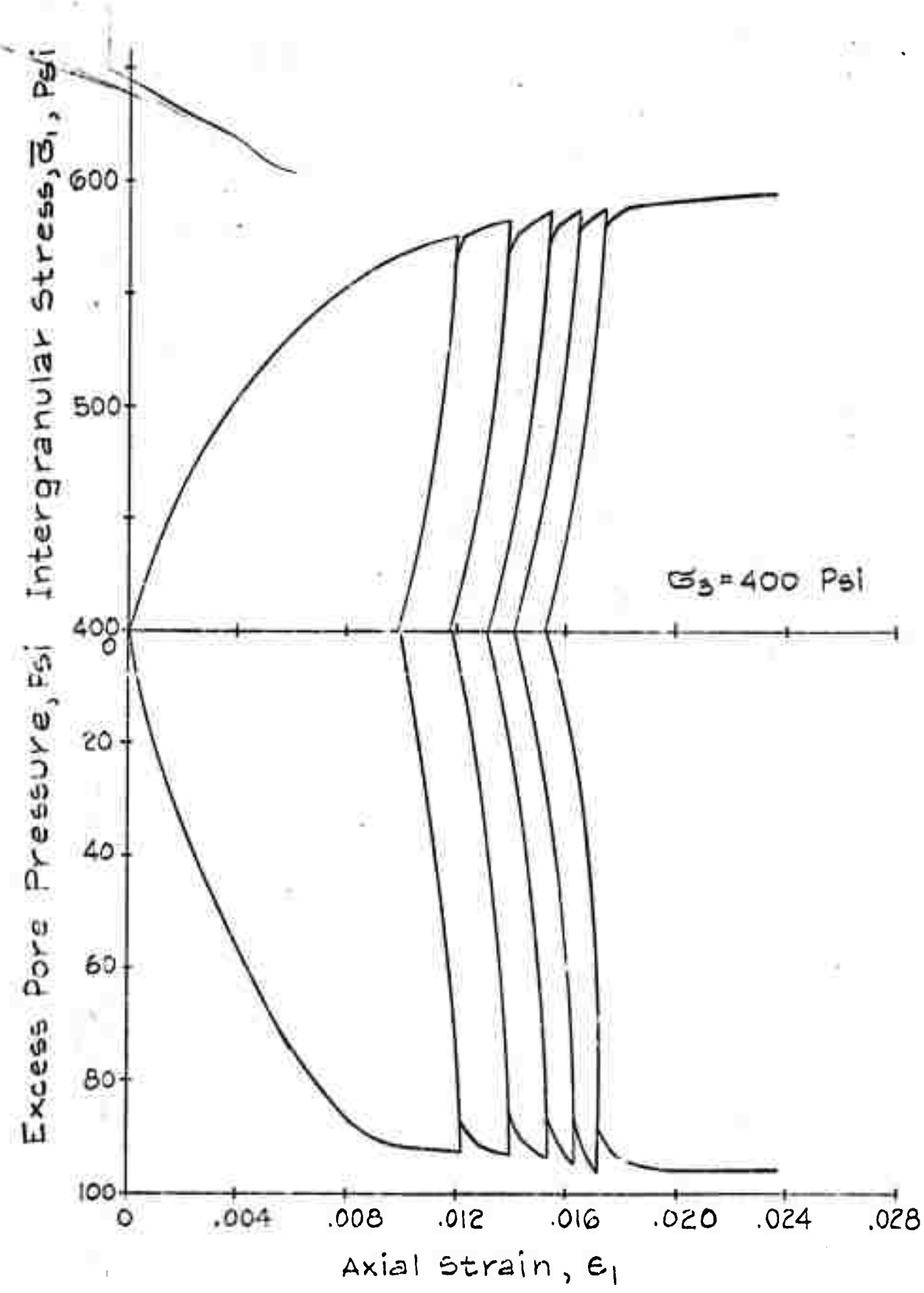

Fig. 21 Triaxial Response, Ranch Sand Model,

Consolidated Undrained Test

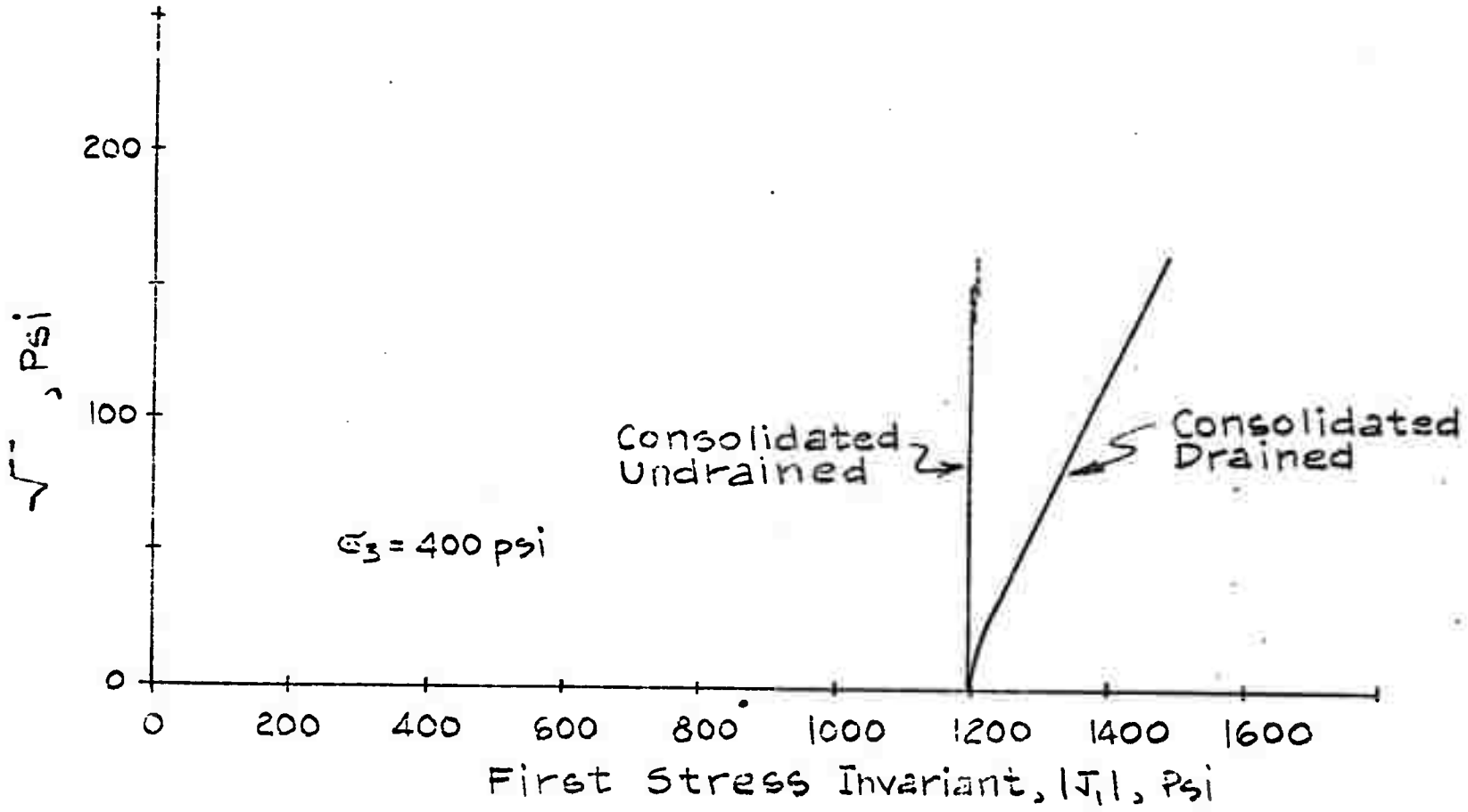

Fig. 22 Triaxial Response, Ranch Sand Model, Effective Stress Invariants

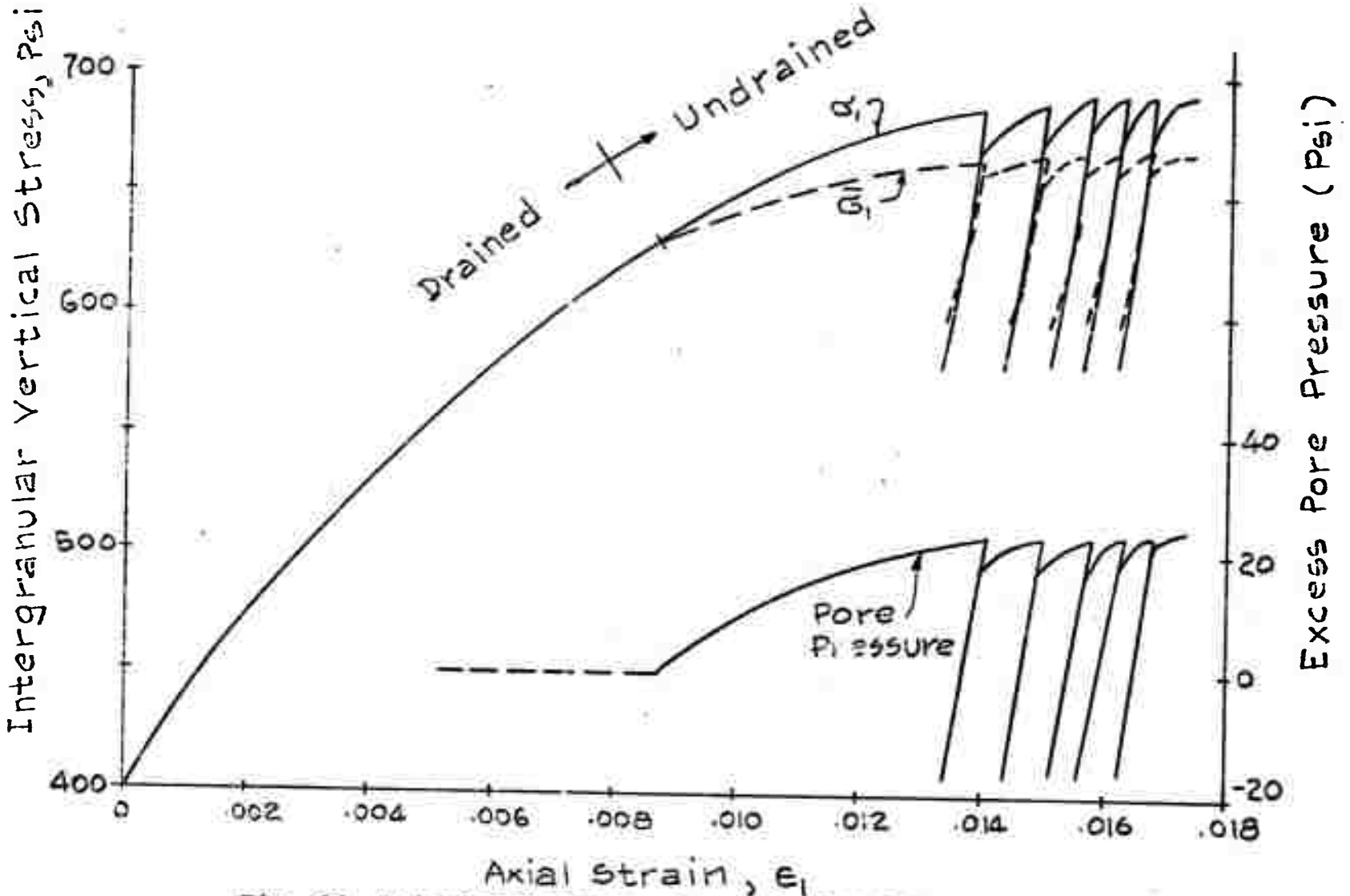

Fig. 23 Triaxial Response, Ranch Sand Model,

Consolidated Drained/Undrained Test

4.0 SUMMARY

Numerical results presented herein fall into two categories. The first set of data presented are concerned with determining the adequacy and characteristics of the numerical solutions for combined stress-seepage. These results indicate that the formulation and the associated computer code developed to treat these problems are complete and debugged. The final set of data is concerned with attempting to evaluate the adequacy of some nonlinear soil constitutive models in predicting soil response to load. The simple Coulomb-Mohr model is clearly inadequate except for some simple problems where strength alone is of interest. However, for those problems where stress-history is significant, the Coulomb-Mohr model must be judged inadequate except possibly to judge gross strength behavior.

The McCormick-Ranch model (or types similar to this) are of course a significant improvement since they will at least reproduce some known experimental responses. It can be anticipated that they would be adequate for various static problems of interest or for those with only one or two load unload cycles. However, these models must be judged inadequate in predicting responses under cyclic loadings such as those encountered in seismic problems. Further experimental data must be developed for loading situations with many cycles.

5.0 REFERENCES

1. C. J. Costantino, "Stress Wave Propagation Through Earth-Water Systems" Interim Report No. 70-409-1, The City College Research Foundation for Advanced Research Projects Agency, Contract No. DAHC 19-69-C-0032, March, 1970.

2. D. W. Taylor, "Fundamentals of Soil Mechanics," John Wiley and Sons, Inc., 1948.

3. D. C. Drucker, W. Prager, "Soil Mechanics and Plastic Analysis or Limit Design," Quarterly of Applied Mathematics, vol. 10, 1952.

4. I. Nelson, "Investigation of Ground Shock Effects in Nonlinear Hysteratic Media; Report No. 2, Modeling The Behavior of a Real Soil," U. S. Army Waterways Experiment Station, Report No. S-68-1, July, 1970.

5. C. J. Costantino, "Two-Dimensional Wave Propagation Through Non-linear Media," Journal of Computational Physics, August, 1969.

6. C. J. Costantino, "Finite Element Approach to Stress Wave Problems," Journal, Engineering Mechanics Division, ASCE, April, 1967.

7. C. J. Costantino, "Stress Waves in Layered Arbitrary Materials," Air Force Space and Missile Systems Organization Report No. SAMSO TR-68-225, September, 1968.

8. O. C. Zienkiewicz, "The Finite Element Method in Engineering Science," McGraw-Hill Book Co., 1971.

APPENDIX A

FORMULATION OF SYSTEM EQUATIONS

In the following presentation, the analysis will be carried forth for a typical element of the free-field mesh. The displacement field for the element is assumed to be linear and the displacement of any point within the element can be written as

$$u(r,z) = \{g\}'\{\alpha\}$$

$$w(r,z) = \{g\}'\{\beta\} \qquad \text{(A.1)}$$

where (u,w) are the horizontal and vertical displacement components and $\{\alpha\}$, $\{\beta\}$ are each a set of arbitrary coefficients, with the number of coefficients equal to the number of element vertices to provide the proper number of degrees of freedom for the element.

The vector $\{g\}$ is formed by a proper set of element functions and depend upon the element type being considered. For a typical triangular element (Fig. A.1) this vector is

$$\{g\} = \{1, r, z\} \qquad \text{(A.2)}$$

while for a typical rectangular element (Fig. A.2)

$$\{g\} = \{1, r, z, rz\} \qquad \text{(A.3)}$$

For a general quadrilateral element (Fig. A.3) the vector $\{g\}$ specified by equation A.3 is used in the transformed coordinate system. By substituting the coordinates of the nodes into equation A.1, the coefficients $\{\alpha\}, \{\beta\}$ can be replaced as unknowns by the node point displacement components, or

$$u(r,z) = \{g\}'[D]\{u\}$$
$$w(r,z) = \{g\}'[D]\{w\} \qquad \text{(A.4)}$$

This simple displacement function assumed for the element allows for determining any interior displacement in terms of the nodal displacements and ensures that the displacements between any two adjacent elements will be continuous for any arbitrary specification of nodal displacements. Higher order element formulations are also available to satisfy the above criteria.

The strains developed at any point within the element can be determined from the strain displacement relations for the particular configuration, or

$$\{\epsilon^T\} = [B_u]\{u\} + [B_w]\{w\} \qquad \text{(A.5)}$$

where $\{\epsilon^T\}$ is the strain vector with components

$$\{\epsilon^T\} = \{\epsilon_r^T, \epsilon_\theta^T, \epsilon_z^T, \gamma_{rz}^T\} \qquad \text{(A.6)}$$

The superscript T in equation A.6 indicates total strains.

For the combined stress/pore pressure problem, the intergranular stress are related to the pore pressure by

$$\{\sigma\} = \{\bar{\sigma}\} - \pi\{I\} \tag{A.7}$$

where $\{\sigma\}$ are the total stress in the body defined by

$$\{\sigma\} = \{\sigma_r, \sigma_\theta, \sigma_z, \tau_{rz}\} \tag{A.8}$$

$\{\bar{\sigma}\}$ are the effective or intergranular stresses and π is the pore pressure. The vector $\{I\}$ is defined as $\{1, 1, 1, 0\}$. The effective stresses are related to the strains through the general stress strain relations

$$\{\bar{\sigma}\} = [C]\{\epsilon^T - \epsilon^N\} \tag{A.9}$$

where $\{\epsilon^N\}$ are defined as the nonlinear components of the total strain and $[C]$ is the usual elastic stress strain matrix which, for example, can be defined for the axisymmetric problem by

$$[C] = \bar{E}\begin{bmatrix} 1-\nu & \nu & \nu & 0 \\ \nu & 1-\nu & \nu & 0 \\ \nu & \nu & 1-\nu & 0 \\ 0 & 0 & 0 & \left(\frac{1-2\nu}{2}\right) \end{bmatrix} \tag{A.10}$$

and $\bar{E} = E/(1+\nu)(1-2\nu)$

where E is Young's modulus and ν is Poisson's ratio. For relatively simple material models (such as The Mises or Coulomb-Mohr plastic models), the nonlinear strains represent the nonrecoverable or plastic strain components. For more complicated material models, the vector $\{\epsilon^N\}$ represents a fictitious set of strains required to yield the proper stresses.

To satisfy equilibrium conditions at the element nodes with the total stress field within the element, the usual virtual work principal is used. The internal work performed by the stresses on a virtual total strain field is defined by

$$\delta W_i = \int_V \{\delta\epsilon^T\}' \{\sigma\}\, dV \tag{A.11}$$

where the integral is taken over the element volume. The corresponding external work performed by forces applied at the nodes is

$$\delta W_e = \{\delta u\}' \{R_u\} + \{\delta w\}' \{R_w\} \tag{A.12}$$

where $\{R_u\}$ are the horizontal force components at each node and $\{R_w\}$ are the corresponding vertical force components. Equating the internal and external work expressions and making us of the definitions previously described, the force components that must be applied at each node point to maintain equilibrium with the total stress within an element are

$$\{R_u\} = [k_{uu}]\{u\} + [k_{uw}]\{w\} - \{R_u^N\} - \{R_u^P\}$$

$$\{R_w\} = [k_{wu}]\{u\} + [k_{ww}]\{w\} - \{R_w^N\} - \{R_w^P\} \qquad \text{(A.13)}$$

The matrices $[k_{uu}]$, $[k_{uw}]$, etc. are the usual elastic stiffness matrices and are defined by

$$[k_{ij}] = \int_V [B_i]'[c][B_j]\, dV \qquad \text{(A.14)}$$

where the subscripts (i,j) take on the values of (u,w). The terms $\{R_u^N\}$, $\{R_w^N\}$ represent the correction forces to account for material nonlinearity and are defined by

$$\{R_i^N\} = \int_V [B_i]'[c]\{\epsilon^N\}\, dV \qquad \text{(A.15)}$$

where again the subscript (i) takes on the values (u,w). The terms $\{R_u^P\}$, $\{R_w^P\}$ represent the effects of pore pressure on the equilibrium equations and are defined by

$$\{R_i^P\} = \int_V \pi [B_i]'\{I\}\, dV \qquad \text{(A.16)}$$

In the computer program developed, the pore pressure variation is assumed to be a linear one over the element or

$$\pi(r,z) = \{g\}'[D]\{\pi\} \qquad \text{(A.17)}$$

where the vector $\{\pi\}$ represents the nodal point pore pressures. Substituting equation A.17 into A.16 then yields

$$\{R_i^p\} = [\bar{k}_i]\{\pi\} \tag{A.18}$$

where $$[\bar{k}_i] = \int_v [B_i]'\{I\}\{g\}'[D]\, dV \tag{A.19}$$

where the subscript i represents both the u and w directions.

To relate the pore presusres to the node point displacements (or velocities), seepage effects are considered. The seepage equations are obtained by minimizing the functional (Ref. 8).

$$\Omega = \int_v \left\{ \frac{1}{2}\left[k_{rr}\left(\frac{\partial \pi}{\partial r}\right)^2 + 2k_{rz}\left(\frac{\partial \pi}{\partial r}\right)\left(\frac{\partial \pi}{\partial z}\right) + k_{zz}\left(\frac{\partial \pi}{\partial z}\right)^2 \right] - \pi Q \right\} dV \tag{A.20}$$

The permeability components k_{rr}, k_{rz}, k_{zz} are related to the principal permeability coefficients by

$$\begin{aligned} k_{rr} &= k_1 \sin^2\theta + k_2 \cos^2\theta \\ k_{rz} &= \sin\theta \cos\theta\, (k_2 - k_1) \\ k_{zz} &= k_1 \cos^2\theta + k_2 \sin^2\theta \end{aligned} \tag{A.21}$$

where (k_1, k_2) are the principal coefficients in two orthogonal directions and θ is the angle from the 1-direction to the r-direction positive in the clockwise sense.

For a particular element, the variation of pore pressure over the element is assumed to be linear or

$$\pi(r,z) = \{g\}'[D]\{\pi\} \tag{A.22}$$

Substituting equation A.22 into A.20, the functional can be written as

$$\Omega = \frac{1}{2}\{\pi\}'[D][S][D]\{\pi\} - \{\pi\}'[D]'\{J\} \tag{A.23}$$

where the matrix $[S]$ is defined by

$$S_{ij} = \int_v \left\{ k_{rr} \frac{\partial g_i}{\partial r}\frac{\partial g_j}{\partial r} + 2k_{rz}\frac{\partial g_i}{\partial r}\frac{\partial g_j}{\partial z} + k_{zz}\frac{\partial g_i}{\partial z}\frac{\partial g_j}{\partial z} \right\} dV \tag{A.24}$$

The vector $\{J\}$ is defined as the volume integrals

$$\{J\} = \int_v Q\{g\}\, dV \tag{A.25}$$

where Q is the volume decrease per unit volume per unit time.

The solution to the seepage problem is obtained by minimizing the function Ω with respect to the nodal pressures leading to the conservation equation

$$[D]'[S][D]\{\pi\} = [D]'\{J\} \tag{A.26}$$

or to further condense notation

$$[H]\{\pi\} = [D]'\{J\} \tag{A.27}$$

The vector $\{J\}$ can be evaluated by considering the volume compression of the solids plus that of the water, or

$$Q = -\{\dot{\epsilon}^T\}'\{I\} + \frac{1}{E_v}\pi \tag{A.28}$$

where E_v is the effective bulk modulus of water and the vector $\{\dot{\epsilon}^T\}$ is the total strain rate vector. The strain rates are related to the nodal velocities by

$$\{\dot{\epsilon}^T\} = [B_u]\{\dot{u}\} + [B_w]\{\dot{w}\} \tag{A.29}$$

Substituting the above into the conservation equation leads to

$$[H]\{\pi\} = -[\bar{k}_u]'\{\dot{u}\} - [\bar{k}_w]'\{\dot{w}\} + [H^*]\{\pi\} \tag{A.30}$$

where $$[H^*] = [D]'[T][D]$$

and $$[T] = \frac{1}{E_v}\int_v \{g\}\{g\}'dV$$

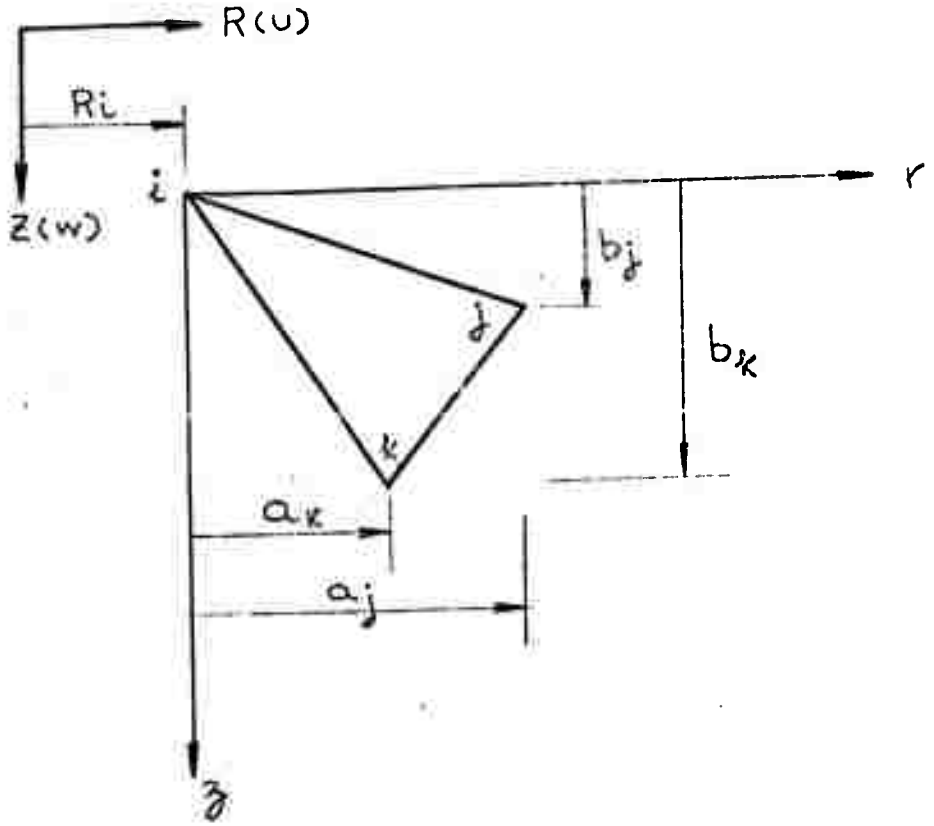

Fig. A.1 General Triangular Element

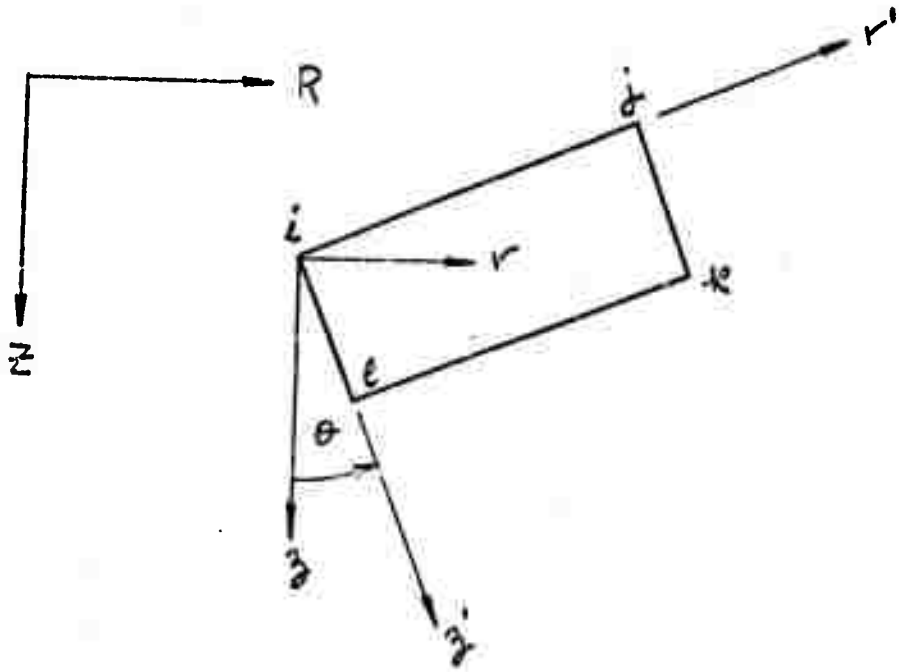

Fig. A.2 General Rectangular Element

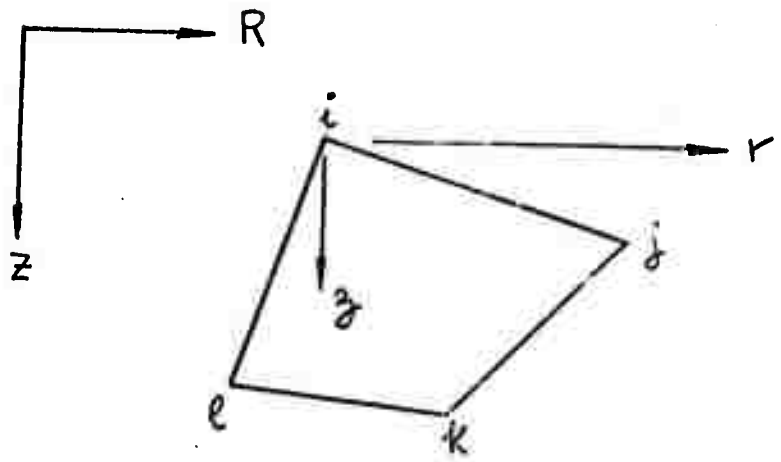

(a) Original Coordinates

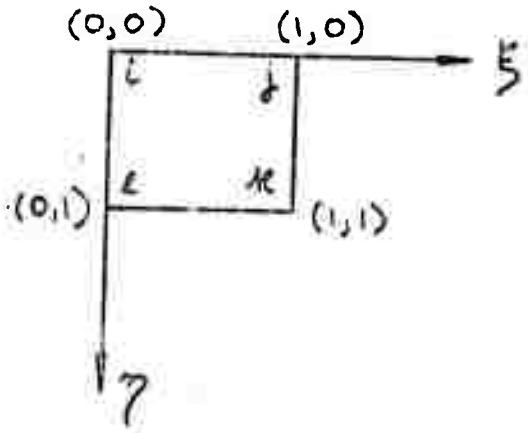

(b) Transformed Coordinates

Fig. A.3 General Quadrilateral Element